

# Chapter 7

## Flow Past Immersed Bodies

**Motivation.** This chapter is devoted to “external” flows around bodies immersed in a fluid stream. Such a flow will have viscous (shear and no-slip) effects near the body surfaces and in its wake, but will typically be nearly inviscid far from the body. These are unconfined *boundary-layer* flows.

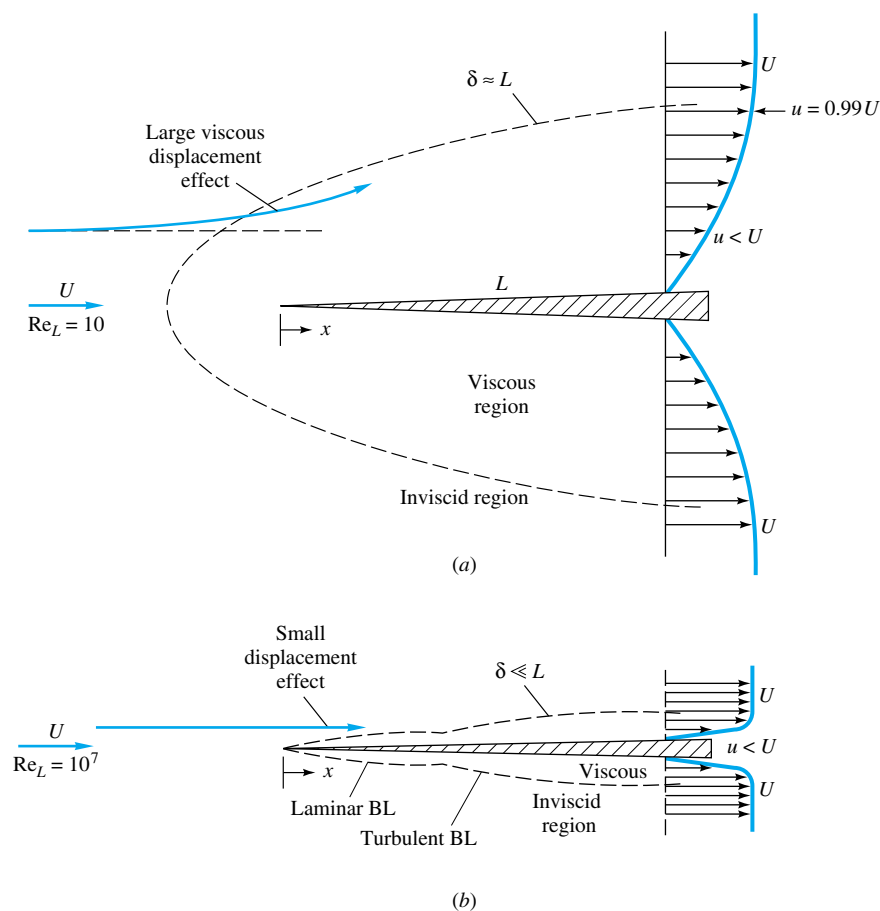
Chapter 6 considered “internal” flows confined by the walls of a duct. In that case the viscous boundary layers grow from the sidewalls, meet downstream, and fill the entire duct. Viscous shear is the dominant effect. For example, the Moody chart of Fig. 6.13 is essentially a correlation of wall shear stress for long ducts of constant cross section.

External flows are unconfined, free to expand no matter how thick the viscous layers grow. Although boundary-layer theory (Sec. 7.3) is helpful in understanding external flows, complex body geometries usually require experimental data on the forces and moments caused by the flow. Such immersed-body flows are commonly encountered in engineering studies: *aerodynamics* (airplanes, rockets, projectiles), *hydrodynamics* (ships, submarines, torpedos), *transportation* (automobiles, trucks, cycles), *wind engineering* (buildings, bridges, water towers, wind turbines), and *ocean engineering* (buoys, breakwaters, pilings, cables, moored instruments). This chapter provides data and analysis to assist in such studies.

### 7.1 Reynolds-Number and Geometry Effects

The technique of boundary-layer (BL) analysis can be used to compute viscous effects near solid walls and to “patch” these onto the outer inviscid motion. This patching is more successful as the body Reynolds number becomes larger, as shown in Fig. 7.1.

In Fig. 7.1 a uniform stream  $U$  moves parallel to a sharp flat plate of length  $L$ . If the Reynolds number  $UL/\nu$  is low (Fig. 7.1a), the viscous region is very broad and extends far ahead and to the sides of the plate. The plate retards the oncoming stream greatly, and small changes in flow parameters cause large changes in the pressure distribution along the plate. Thus, although in principle it should be possible to patch the



**Fig. 7.1** Comparison of flow past a sharp flat plate at low and high Reynolds numbers: (a) laminar, low-Re flow; (b) high-Re flow.

viscous and inviscid layers in a mathematical analysis, their interaction is strong and nonlinear [1 to 3]. There is no existing simple theory for external-flow analysis at Reynolds numbers from 1 to about 1000. Such thick-shear-layer flows are typically studied by experiment or by numerical modeling of the flow field on a digital computer [4].

A high-Reynolds-number flow (Fig. 7.1b) is much more amenable to boundary-layer patching, as first pointed out by Prandtl in 1904. The viscous layers, either laminar or turbulent, are very thin, thinner even than the drawing shows. We define the boundary-layer thickness  $\delta$  as the locus of points where the velocity  $u$  parallel to the plate reaches 99 percent of the external velocity  $U$ . As we shall see in Sec. 7.4, the accepted formulas for flat-plate flow are

$$\frac{\delta}{x} \approx \begin{cases} \frac{5.0}{Re_x^{1/2}} & \text{laminar} \\ \frac{0.16}{Re_x^{1/7}} & \text{turbulent} \end{cases} \quad (7.1a) \quad (7.1b)$$

where  $Re_x = Ux/\nu$  is called the *local Reynolds number* of the flow along the plate surface. The turbulent-flow formula applies for  $Re_x$  greater than approximately  $10^6$ .

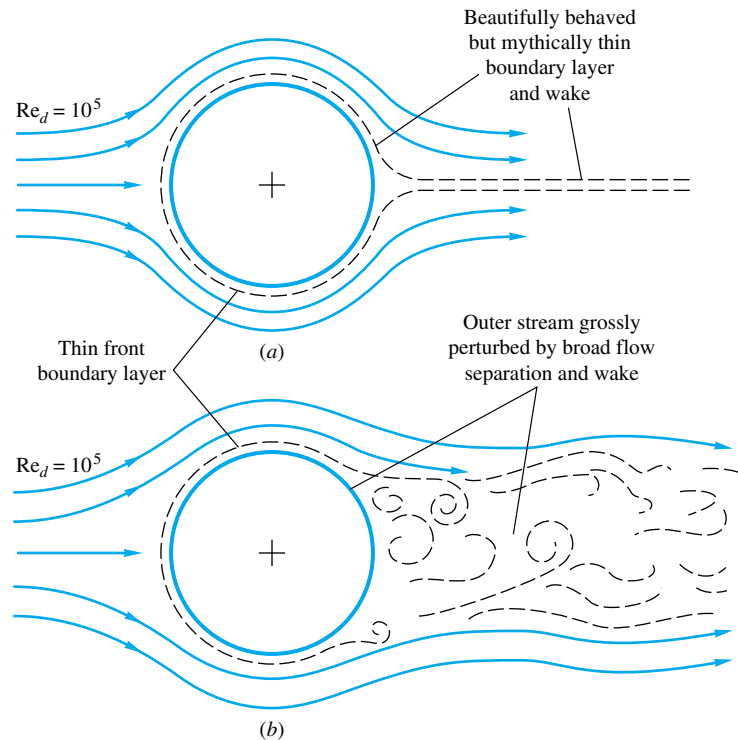
Some computed values from Eq. (7.1) are

| $Re_x$                     | $10^4$ | $10^5$ | $10^6$ | $10^7$ | $10^8$ |
|----------------------------|--------|--------|--------|--------|--------|
| $(\delta/x)_{\text{lam}}$  | 0.050  | 0.016  | 0.005  |        |        |
| $(\delta/x)_{\text{turb}}$ |        |        | 0.022  | 0.016  | 0.011  |

The blanks indicate that the formula is not applicable. In all cases these boundary layers are so thin that their displacement effect on the outer inviscid layer is negligible. Thus the pressure distribution along the plate can be computed from inviscid theory as if the boundary layer were not even there. This external pressure field then “drives” the boundary-layer flow, acting as a forcing function in the momentum equation along the surface. We shall explain this boundary-layer theory in Secs. 7.4 and 7.5.

For slender bodies, such as plates and airfoils parallel to the oncoming stream, we conclude that this assumption of negligible interaction between the boundary layer and the outer pressure distribution is an excellent approximation.

For a blunt-body flow, however, even at very high Reynolds numbers, there is a discrepancy in the viscous-inviscid patching concept. Figure 7.2 shows two sketches of flow past a two- or three-dimensional blunt body. In the idealized sketch (7.2a), there is a thin film of boundary layer about the body and a narrow sheet of viscous wake in the rear. The patching theory would be glorious for this picture, but it is false. In the



**Fig. 7.2** Illustration of the strong interaction between viscous and inviscid regions in the rear of blunt-body flow: (a) idealized and definitely false picture of blunt-body flow; (b) actual picture of blunt-body flow.

actual flow (Fig. 7.2*b*), the boundary layer is thin on the front, or windward, side of the body, where the pressure decreases along the surface (*favorable* pressure gradient). But in the rear the boundary layer encounters increasing pressure (*adverse* pressure gradient) and breaks off, or separates, into a broad, pulsating wake. (See Fig. 5.2*a* for a photograph of a specific example.) The mainstream is deflected by this wake, so that the external flow is quite different from the prediction from inviscid theory with the addition of a thin boundary layer.

The theory of strong interaction between blunt-body viscous and inviscid layers is not well developed. Flows like that of Fig. 7.2*b* are normally studied experimentally. Reference 5 is an example of efforts to improve the theory of separated-boundary-layer flows. Reference 6 is a textbook devoted to separated flow.

---

### EXAMPLE 7.1

---

A long, thin flat plate is placed parallel to a 20-ft/s stream of water at 20°C. At what distance  $x$  from the leading edge will the boundary-layer thickness be 1 in?

---

#### Solution

---

Since we do not know the Reynolds number, we must guess which of Eqs. (7.1) applies. From Table 1.4 for water,  $\nu = 1.09 \times 10^{-5} \text{ ft}^2/\text{s}$ ; hence

$$\frac{U}{\nu} = \frac{20 \text{ ft/s}}{1.09 \times 10^{-5} \text{ ft}^2/\text{s}} = 1.84 \times 10^6 \text{ ft}^{-1}$$

With  $\delta = 1 \text{ in} = \frac{1}{12} \text{ ft}$ , try Eq. (7.1*a*):

$$\text{Laminar flow:} \quad \frac{\delta}{x} = \frac{5}{(Ux/\nu)^{1/2}}$$

$$\text{or} \quad x = \frac{\delta^2(U/\nu)}{5^2} = \frac{(\frac{1}{12} \text{ ft})^2(1.84 \times 10^6 \text{ ft}^{-1})}{25} = 511 \text{ ft}$$

Now we can test the Reynolds number to see whether the formula applied:

$$\text{Re}_x = \frac{Ux}{\nu} = \frac{(20 \text{ ft/s})(511 \text{ ft})}{1.09 \times 10^{-5} \text{ ft}^2/\text{s}} = 9.4 \times 10^8$$

This is impossible since the maximum  $\text{Re}_x$  for laminar flow past a flat plate is  $3 \times 10^6$ . So we try again with Eq. (7.1*b*):

$$\text{Turbulent flow:} \quad \frac{\delta}{x} = \frac{0.16}{(Ux/\nu)^{1/7}}$$

$$\text{or} \quad x = \left[ \frac{\delta(U/\nu)^{1/7}}{0.16} \right]^{7/6} = \left[ \frac{(\frac{1}{12} \text{ ft})(1.84 \times 10^6 \text{ ft}^{-1})^{1/7}}{0.16} \right]^{7/6} = (4.09)^{7/6} = 5.17 \text{ ft} \quad \text{Ans.}$$

$$\text{Test} \quad \text{Re}_x = \frac{(20 \text{ ft/s})(5.17 \text{ ft})}{1.09 \times 10^{-5} \text{ ft}^2/\text{s}} = 9.5 \times 10^6$$

This is a perfectly proper turbulent-flow condition; hence we have found the correct position  $x$  on our second try.

---

## 7.2 Momentum-Integral Estimates

When we derived the momentum-integral relation, Eq. (3.37), and applied it to a flat-plate boundary layer in Example 3.11, we promised to consider it further in Chap. 7. Well, here we are! Let us review the problem, using Fig. 7.3.

A shear layer of unknown thickness grows along the sharp flat plate in Fig. 7.3. The no-slip wall condition retards the flow, making it into a rounded profile  $u(y)$ , which merges into the external velocity  $U = \text{constant}$  at a “thickness”  $y = \delta(x)$ . By utilizing the control volume of Fig. 3.11, we found (without making any assumptions about laminar versus turbulent flow) in Example 3.11 that the drag force on the plate is given by the following momentum integral across the exit plane

$$D(x) = \rho b \int_0^{\delta(x)} u(U - u) dy \quad (7.2)$$

where  $b$  is the plate width into the paper and the integration is carried out along a vertical plane  $x = \text{constant}$ . You should review the momentum-integral relation (3.37) and its use in Example 3.11.

### Kármán’s Analysis of the Flat Plate

Equation (7.2) was derived in 1921 by Kármán [7], who wrote it in the convenient form of the *momentum thickness*  $\theta$

$$D(x) = \rho b U^2 \theta \quad \theta = \int_0^{\delta} \frac{u}{U} \left( 1 - \frac{u}{U} \right) dy \quad (7.3)$$

Momentum thickness is thus a measure of total plate drag. Kármán then noted that the drag also equals the integrated wall shear stress along the plate

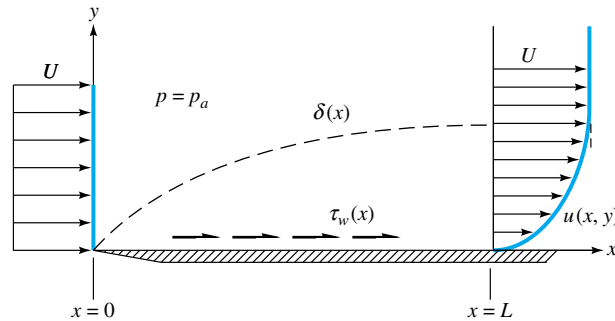
$$D(x) = b \int_0^x \tau_w(x) dx$$

$$\text{or} \quad \frac{dD}{dx} = b \tau_w \quad (7.4)$$

Meanwhile, the derivative of Eq. (7.3), with  $U = \text{constant}$ , is

$$\frac{dD}{dx} = \rho b U^2 \frac{d\theta}{dx}$$

By comparing this with Eq. (7.4) Kármán arrived at what is now called the *momentum-integral relation* for flat-plate boundary-layer flow



**Fig. 7.3** Growth of a boundary layer on a flat plate.

$$\tau_w = \rho U^2 \frac{d\theta}{dx} \quad (7.5)$$

It is valid for either laminar or turbulent flat-plate flow.

To get a numerical result for laminar flow, Kármán assumed that the velocity profiles had an approximately parabolic shape

$$u(x, y) \approx U \left( \frac{2y}{\delta} - \frac{y^2}{\delta^2} \right) \quad 0 \leq y \leq \delta(x) \quad (7.6)$$

which makes it possible to estimate both momentum thickness and wall shear

$$\begin{aligned} \theta &= \int_0^\delta \left( \frac{2y}{\delta} - \frac{y^2}{\delta^2} \right) \left( 1 - \frac{2y}{\delta} + \frac{y^2}{\delta^2} \right) dy \approx \frac{2}{15} \delta \\ \tau_w &= \mu \left. \frac{\partial u}{\partial y} \right|_{y=0} \approx \frac{2\mu U}{\delta} \end{aligned} \quad (7.7)$$

By substituting (7.7) into (7.5) and rearranging we obtain

$$\delta \, d\delta \approx 15 \frac{\nu}{U} dx \quad (7.8)$$

where  $\nu = \mu/\rho$ . We can integrate from 0 to  $x$ , assuming that  $\delta = 0$  at  $x = 0$ , the leading edge

$$\frac{1}{2} \delta^2 = \frac{15\nu x}{U}$$

$$\text{or} \quad \frac{\delta}{x} \approx 5.5 \left( \frac{\nu}{Ux} \right)^{1/2} = \frac{5.5}{\text{Re}_x^{1/2}} \quad (7.9)$$

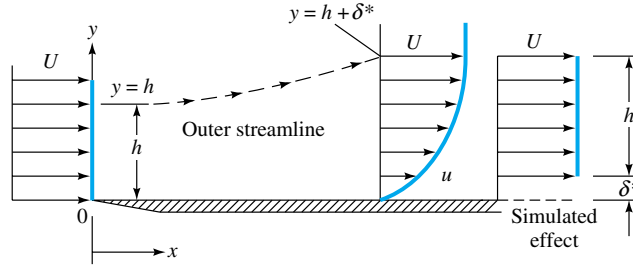
This is the desired thickness estimate. It is all approximate, of course, part of Kármán's *momentum-integral theory* [7], but it is startlingly accurate, being only 10 percent higher than the known exact solution for laminar flat-plate flow, which we gave as Eq. (7.1a).

By combining Eqs. (7.9) and (7.7) we also obtain a shear-stress estimate along the plate

$$c_f = \frac{2\tau_w}{\rho U^2} \approx \left( \frac{\frac{8}{15}}{\text{Re}_x} \right)^{1/2} = \frac{0.73}{\text{Re}_x^{1/2}} \quad (7.10)$$

Again this estimate, in spite of the crudeness of the profile assumption (7.6) is only 10 percent higher than the known exact laminar-plate-flow solution  $c_f = 0.664/\text{Re}_x^{1/2}$ , treated in Sec. 7.4. The dimensionless quantity  $c_f$ , called the *skin-friction coefficient*, is analogous to the friction factor  $f$  in ducts.

A boundary layer can be judged as “thin” if, say, the ratio  $\delta/x$  is less than about 0.1. This occurs at  $\delta/x = 0.1 = 5.0/\text{Re}_x^{1/2}$  or at  $\text{Re}_x = 2500$ . For  $\text{Re}_x$  less than 2500 we can estimate that boundary-layer theory fails because the thick layer has a significant effect on the outer inviscid flow. The upper limit on  $\text{Re}_x$  for laminar flow is about  $3 \times 10^6$ , where measurements on a smooth flat plate [8] show that the flow undergoes transition to a turbulent boundary layer. From  $3 \times 10^6$  upward the turbulent Reynolds number may be arbitrarily large, and a practical limit at present is  $5 \times 10^9$  for oil supertankers.



**Fig. 7.4** Displacement effect of a boundary layer.

### Displacement Thickness

Another interesting effect of a boundary layer is its small but finite displacement of the outer streamlines. As shown in Fig. 7.4, outer streamlines must deflect outward a distance  $\delta^*(x)$  to satisfy conservation of mass between the inlet and outlet

$$\int_0^h \rho U b \, dy = \int_0^\delta \rho u b \, dy \quad \delta = h + \delta^* \quad (7.11)$$

The quantity  $\delta^*$  is called the *displacement thickness* of the boundary layer. To relate it to  $u(y)$ , cancel  $\rho$  and  $b$  from Eq. (7.11), evaluate the left integral, and slyly add and subtract  $U$  from the right integrand:

$$Uh = \int_0^\delta (U + u - U) \, dy = U(h + \delta^*) + \int_0^\delta (u - U) \, dy$$

$$\text{or} \quad \delta^* = \int_0^\delta \left(1 - \frac{u}{U}\right) \, dy \quad (7.12)$$

Thus the ratio of  $\delta^*/\delta$  varies only with the dimensionless velocity-profile shape  $u/U$ .

Introducing our profile approximation (7.6) into (7.12), we obtain by integration the approximate result

$$\delta^* \approx \frac{1}{3} \delta \quad \frac{\delta^*}{x} \approx \frac{1.83}{\text{Re}_x^{1/2}} \quad (7.13)$$

These estimates are only 6 percent away from the exact solutions for laminar flat-plate flow given in Sec. 7.4:  $\delta^* = 0.344\delta = 1.721x/\text{Re}_x^{1/2}$ . Since  $\delta^*$  is much smaller than  $x$  for large  $\text{Re}_x$  and the outer streamline slope  $V/U$  is proportional to  $\delta^*$ , we conclude that the velocity normal to the wall is much smaller than the velocity parallel to the wall. This is a key assumption in boundary-layer theory (Sec. 7.3).

We also conclude from the success of these simple parabolic estimates that Kármán's momentum-integral theory is effective and useful. Many details of this theory are given in Refs. 1 to 3.

### EXAMPLE 7.2

Are low-speed, small-scale air and water boundary layers really thin? Consider flow at  $U = 1$  ft/s past a flat plate 1 ft long. Compute the boundary-layer thickness at the trailing edge for (a) air and (b) water at 20°C.

---

**Solution**


---

**Part (a)** From Table A.3,  $\nu_{\text{air}} \approx 1.61 \text{ E-4 ft}^2/\text{s}$ . The trailing-edge Reynolds number thus is

$$\text{Re}_L = \frac{UL}{\nu} = \frac{(1 \text{ ft/s})(1 \text{ ft})}{1.61 \text{ E-4 ft}^2/\text{s}} = 6200$$

Since this is less than  $10^6$ , the flow is presumed laminar, and since it is greater than 2500, the boundary layer is reasonably thin. From Eq. (7.1a), the predicted laminar thickness is

$$\frac{\delta}{x} \approx \frac{5.0}{\sqrt{6200}} = 0.0634$$

or, at  $x = 1 \text{ ft}$ ,  $\delta = 0.0634 \text{ ft} \approx 0.76 \text{ in}$  *Ans. (a)*

**Part (b)** From Table A.2  $\nu_{\text{water}} \approx 1.08 \text{ E-5 ft}^2/\text{s}$ . The trailing-edge Reynolds number is

$$\text{Re}_L = \frac{(1 \text{ ft/s})(1 \text{ ft})}{1.08 \text{ E-5 ft}^2/\text{s}} \approx 92,600$$

This again satisfies the laminar and thinness conditions. The boundary-layer thickness is

$$\frac{\delta}{x} \approx \frac{5.0}{\sqrt{92,600}} = 0.0164$$

or, at  $x = 1 \text{ ft}$ ,  $\delta = 0.0164 \text{ ft} \approx 0.20 \text{ in}$  *Ans. (b)*

Thus, even at such low velocities and short lengths, both airflows and water flows satisfy the boundary-layer approximations.

---

## 7.3 The Boundary-Layer Equations

In Chaps. 4 and 6 we learned that there are several dozen known analytical laminar-flow solutions [1 to 3]. None are for external flow around immersed bodies, although this is one of the primary applications of fluid mechanics. No exact solutions are known for turbulent flow, whose analysis typically uses empirical modeling laws to relate time-mean variables.

There are presently three techniques used to study external flows: (1) numerical (digital-computer) solutions, (2) experimentation, and (3) boundary-layer theory.

*Computational fluid dynamics* (CFD) is now well developed and described in advanced texts such as that by Anderson et al. [4]. Thousands of computer solutions and models have been published; execution times, mesh sizes, and graphical presentations are improving each year. Both laminar- and turbulent-flow solutions have been published, and turbulence modeling is a current research topic [9]. Except for a brief discussion of computer analysis in Chap. 8, the topic of CFD is beyond our scope here.

Experimentation is the most common method of studying external flows. Chapter 5 outlined the technique of dimensional analysis, and we shall give many nondimensional experimental data for external flows in Sec. 7.6.

The third tool is boundary-layer theory, first formulated by Ludwig Prandtl in 1904. We shall follow Prandtl's ideas here and make certain order-of-magnitude assumptions to greatly simplify the Navier-Stokes equations (4.38) into boundary-layer equations which are solved relatively easily and patched onto the outer inviscid-flow field.



One of the great achievements of boundary-layer theory is its ability to predict the flow separation illustrated in Fig. 7.2*b*. Before 1904 no one realized that such thin shear layers could cause such a gross effect as flow separation. Unfortunately, even today theory cannot accurately predict the behavior of the separated-flow region and its interaction with the outer layer. This is the weakness of boundary-layer theory, which we hope will be overcome by intensive research into the dynamics of separated flows [6].

### Derivation for Two-Dimensional Flow

We consider only steady two-dimensional incompressible viscous flow with the  $x$  direction along the wall and  $y$  normal to the wall, as in Fig. 7.3.<sup>1</sup> We neglect gravity, which is important only in boundary layers where fluid buoyancy is dominant [2, sec. 4.13]. From Chap. 4, the complete equations of motion consist of continuity and the  $x$ - and  $y$ -momentum relations

$$\frac{\partial u}{\partial x} + \frac{\partial v}{\partial y} = 0 \quad (7.14a)$$

$$\rho \left( u \frac{\partial u}{\partial x} + v \frac{\partial u}{\partial y} \right) = -\frac{\partial p}{\partial x} + \mu \left( \frac{\partial^2 u}{\partial x^2} + \frac{\partial^2 u}{\partial y^2} \right) \quad (7.14b)$$

$$\rho \left( u \frac{\partial v}{\partial x} + v \frac{\partial v}{\partial y} \right) = -\frac{\partial p}{\partial y} + \mu \left( \frac{\partial^2 v}{\partial x^2} + \frac{\partial^2 v}{\partial y^2} \right) \quad (7.14c)$$

These should be solved for  $u$ ,  $v$ , and  $p$  subject to typical no-slip, inlet, and exit boundary conditions, but in fact they are too difficult to handle for most external flows.

In 1904 Prandtl correctly deduced that a shear layer must be very thin if the Reynolds number is large, so that the following approximations apply:

$$\text{Velocities:} \quad v \ll u \quad (7.15a)$$

$$\text{Rates of change:} \quad \frac{\partial u}{\partial x} \ll \frac{\partial u}{\partial y} \quad \frac{\partial v}{\partial x} \ll \frac{\partial v}{\partial y} \quad (7.15b)$$

Our discussion of displacement thickness in the previous section was intended to justify these assumptions.

Applying these approximations to Eq. (7.14c) results in a powerful simplification

$$\frac{\partial p}{\partial y} \approx 0 \quad \text{or} \quad p \approx p(x) \text{ only} \quad (7.16)$$

In other words, the  $y$ -momentum equation can be neglected entirely, and the pressure varies only *along* the boundary layer, not through it. The pressure-gradient term in Eq. (7.14b) is assumed to be known in advance from Bernoulli's equation applied to the outer inviscid flow

$$\frac{\partial p}{\partial x} = \frac{dp}{dx} = -\rho U \frac{dU}{dx} \quad (7.17)$$

<sup>1</sup>For a curved wall,  $x$  can represent the arc length along the wall and  $y$  can be everywhere normal to  $x$  with negligible change in the boundary-layer equations as long as the radius of curvature of the wall is large compared with the boundary-layer thickness [1 to 3].

Presumably we have already made the inviscid analysis and know the distribution of  $U(x)$  along the wall (Chap. 8).

Meanwhile, one term in Eq. (7.14b) is negligible due to Eqs. (7.15)

$$\frac{\partial^2 u}{\partial x^2} \ll \frac{\partial^2 u}{\partial y^2} \quad (7.18)$$

However, neither term in the continuity relation (7.14a) can be neglected—another warning that continuity is always a vital part of any fluid-flow analysis.

The net result is that the three full equations of motion (7.14) are reduced to Prandtl's two boundary-layer equations

$$\text{Continuity:} \quad \frac{\partial u}{\partial x} + \frac{\partial v}{\partial y} = 0 \quad (7.19a)$$

$$\text{Momentum along wall:} \quad u \frac{\partial u}{\partial x} + v \frac{\partial u}{\partial y} \approx U \frac{dU}{dx} + \frac{1}{\rho} \frac{\partial \tau}{\partial y} \quad (7.19b)$$

$$\text{where} \quad \tau = \begin{cases} \mu \frac{\partial u}{\partial y} & \text{laminar flow} \\ \mu \frac{\partial u}{\partial y} - \rho \overline{u'v'} & \text{turbulent flow} \end{cases}$$

These are to be solved for  $u(x, y)$  and  $v(x, y)$ , with  $U(x)$  assumed to be a known function from the outer inviscid-flow analysis. There are two boundary conditions on  $u$  and one on  $v$ :

$$\text{At } y = 0 \text{ (wall):} \quad u = v = 0 \quad (\text{no slip}) \quad (7.20a)$$

$$\text{At } y = \delta(x) \text{ (outer stream):} \quad u = U(x) \quad (\text{patching}) \quad (7.20b)$$

Unlike the Navier-Stokes equations (7.14), which are mathematically elliptic and must be solved simultaneously over the entire flow field, the boundary-layer equations (7.19) are mathematically parabolic and are solved by beginning at the leading edge and marching downstream as far as you like, stopping at the separation point or earlier if you prefer.<sup>2</sup>

The boundary-layer equations have been solved for scores of interesting cases of internal and external flow for both laminar and turbulent flow, utilizing the inviscid distribution  $U(x)$  appropriate to each flow. Full details of boundary-layer theory and results and comparison with experiment are given in Refs. 1 to 3. Here we shall confine ourselves primarily to flat-plate solutions (Sec. 7.4).

## 7.4 The Flat-Plate Boundary Layer

The classic and most often used solution of boundary-layer theory is for flat-plate flow, as in Fig. 7.3, which can represent either laminar or turbulent flow.

<sup>2</sup>For further mathematical details, see Ref. 2, sec. 2.8.

## Laminar Flow

For laminar flow past the plate, the boundary-layer equations (7.19) can be solved exactly for  $u$  and  $v$ , assuming that the free-stream velocity  $U$  is constant ( $dU/dx = 0$ ). The solution was given by Prandtl's student Blasius, in his 1908 dissertation from Göttingen. With an ingenious coordinate transformation, Blasius showed that the dimensionless velocity profile  $u/U$  is a function only of the single composite dimensionless variable  $(y)[U/(\nu x)]^{1/2}$ :

$$\frac{u}{U} = f'(\eta) \quad \eta = y \left( \frac{U}{\nu x} \right)^{1/2} \quad (7.21)$$

where the prime denotes differentiation with respect to  $\eta$ . Substitution of (7.21) into the boundary-layer equations (7.19) reduces the problem, after much algebra, to a single third-order nonlinear ordinary differential equation for  $f$

$$f''' + \frac{1}{2}ff'' = 0 \quad (7.22)$$

The boundary conditions (7.20) become

$$\text{At } y = 0: \quad f(0) = f'(0) = 0 \quad (7.23a)$$

$$\text{As } y \rightarrow \infty: \quad f'(\infty) \rightarrow 1.0 \quad (7.23b)$$

This is the *Blasius equation*, for which accurate solutions have been obtained only by numerical integration. Some tabulated values of the velocity-profile shape  $f'(\eta) = u/U$  are given in Table 7.1.

Since  $u/U$  approaches 1.0 only as  $y \rightarrow \infty$ , it is customary to select the boundary-layer thickness  $\delta$  as that point where  $u/U = 0.99$ . From the table, this occurs at  $\eta \approx 5.0$ :

$$\delta_{99\%} \left( \frac{U}{\nu x} \right)^{1/2} \approx 5.0$$

$$\text{or} \quad \frac{\delta}{x} \approx \frac{5.0}{\text{Re}_x^{1/2}} \quad \text{Blasius (1908)} \quad (7.24)$$

**Table 7.1** The Blasius Velocity Profile [1 to 3]

| $y[U/(\nu x)]^{1/2}$ | $u/U$   | $y[U/(\nu x)]^{1/2}$ | $u/U$   |
|----------------------|---------|----------------------|---------|
| 0.0                  | 0.0     | 2.8                  | 0.81152 |
| 0.2                  | 0.06641 | 3.0                  | 0.84605 |
| 0.4                  | 0.13277 | 3.2                  | 0.87609 |
| 0.6                  | 0.19894 | 3.4                  | 0.90177 |
| 0.8                  | 0.26471 | 3.6                  | 0.92333 |
| 1.0                  | 0.32979 | 3.8                  | 0.94112 |
| 1.2                  | 0.39378 | 4.0                  | 0.95552 |
| 1.4                  | 0.45627 | 4.2                  | 0.96696 |
| 1.6                  | 0.51676 | 4.4                  | 0.97587 |
| 1.8                  | 0.57477 | 4.6                  | 0.98269 |
| 2.0                  | 0.62977 | 4.8                  | 0.98779 |
| 2.2                  | 0.68132 | 5.0                  | 0.99155 |
| 2.4                  | 0.72899 | $\infty$             | 1.00000 |
| 2.6                  | 0.77246 |                      |         |

With the profile known, Blasius, of course, could also compute the wall shear and displacement thickness

$$c_f = \frac{0.664}{\text{Re}_x^{1/2}} \quad \frac{\delta^*}{x} = \frac{1.721}{\text{Re}_x^{1/2}} \quad (7.25)$$

Notice how close these are to our integral estimates, Eqs. (7.9), (7.10), and (7.13). When  $c_f$  is converted to dimensional form, we have

$$\tau_w(x) = \frac{0.332\rho^{1/2}\mu^{1/2}U^{1.5}}{x^{1/2}}$$

The wall shear drops off with  $x^{1/2}$  because of boundary-layer growth and varies as velocity to the 1.5 power. This is in contrast to laminar pipe flow, where  $\tau_w \propto U$  and is independent of  $x$ .

If  $\tau_w(x)$  is substituted into Eq. (7.4), we compute the total drag force

$$D(x) = b \int_0^x \tau_w(x) dx = 0.664b\rho^{1/2}\mu^{1/2}U^{1.5}x^{1/2} \quad (7.26)$$

The drag increases only as the square root of the plate length. The nondimensional *drag coefficient* is defined as

$$C_D = \frac{2D(L)}{\rho U^2 bL} = \frac{1.328}{\text{Re}_L^{1/2}} = 2c_f(L) \quad (7.27)$$

Thus, for laminar plate flow,  $C_D$  equals twice the value of the skin-friction coefficient at the trailing edge. This is the drag on one side of the plate.

Kármán pointed out that the drag could also be computed from the momentum relation (7.2). In dimensionless form, Eq. (7.2) becomes

$$C_D = \frac{2}{L} \int_0^\delta \frac{u}{U} \left(1 - \frac{u}{U}\right) dy \quad (7.28)$$

This can be rewritten in terms of the momentum thickness at the trailing edge

$$C_D = \frac{2\theta(L)}{L} \quad (7.29)$$

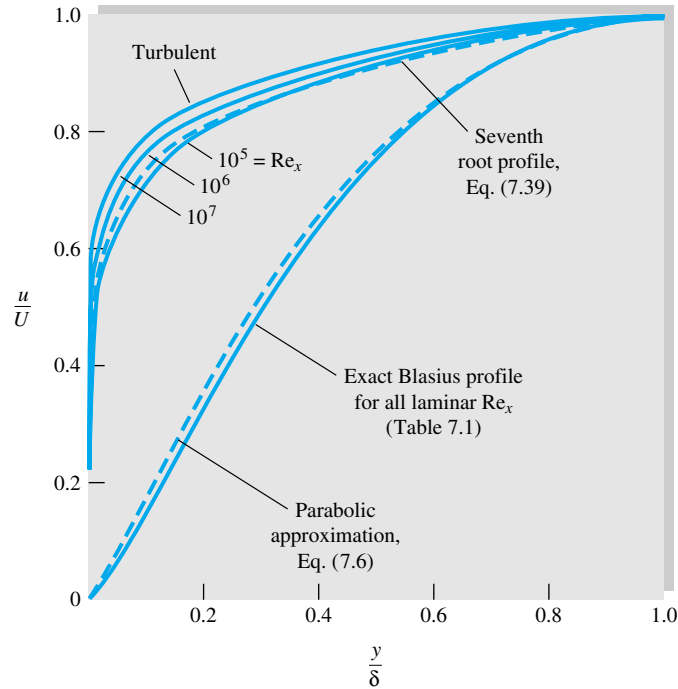
Computation of  $\theta$  from the profile  $u/U$  or from  $C_D$  gives

$$\frac{\theta}{x} = \frac{0.664}{\text{Re}_x^{1/2}} \quad \text{laminar flat plate} \quad (7.30)$$

Since  $\delta$  is so ill defined, the momentum thickness, being definite, is often used to correlate data taken for a variety of boundary layers under differing conditions. The ratio of displacement to momentum thickness, called the dimensionless-profile *shape factor*, is also useful in integral theories. For laminar flat-plate flow

$$H = \frac{\delta^*}{\theta} = \frac{1.721}{0.664} = 2.59 \quad (7.31)$$

A large shape factor then implies that boundary-layer separation is about to occur.



**Fig. 7.5** Comparison of dimensionless laminar and turbulent flat-plate velocity profiles.

If we plot the Blasius velocity profile from Table 7.1 in the form of  $u/U$  versus  $y/\delta$ , we can see why the simple integral-theory guess, Eq. (7.6), was such a great success. This is done in Fig. 7.5. The simple parabolic approximation is not far from the true Blasius profile; hence its momentum thickness is within 10 percent of the true value. Also shown in Fig. 7.5 are three typical turbulent flat-plate velocity profiles. Notice how strikingly different in shape they are from the laminar profiles. Instead of decreasing monotonically to zero, the turbulent profiles are very flat and then drop off sharply at the wall. As you might guess, they follow the logarithmic-law shape and thus can be analyzed by momentum-integral theory if this shape is properly represented.

### Transition to Turbulence

The laminar flat-plate boundary layer eventually becomes turbulent, but there is no unique value for this change to occur. With care in polishing the wall and keeping the free stream quiet, one can delay the transition Reynolds number to  $Re_{x,tr} \approx 3 \text{ E}6$  [8]. However, for typical commercial surfaces and gusty free streams, a more realistic value is  $Re_{x,tr} \approx 5 \text{ E}5$ .

### EXAMPLE 7.3

A sharp flat plate with  $L = 1 \text{ m}$  and  $b = 3 \text{ m}$  is immersed parallel to a stream of velocity  $2 \text{ m/s}$ . Find the drag on one side of the plate, and at the trailing edge find the thicknesses  $\delta$ ,  $\delta^*$ , and  $\theta$  for (a) air,  $\rho = 1.23 \text{ kg/m}^3$  and  $\nu = 1.46 \times 10^{-5} \text{ m}^2/\text{s}$ , and (b) water,  $\rho = 1000 \text{ kg/m}^3$  and  $\nu = 1.02 \times 10^{-6} \text{ m}^2/\text{s}$ .

---

**Solution**


---

**Part (a)** The airflow Reynolds number is

$$\frac{VL}{\nu} = \frac{(2.0 \text{ m/s})(1.0 \text{ m})}{1.46 \times 10^{-5} \text{ m}^2/\text{s}} = 137,000$$

Since this is less than  $3 \times 10^6$ , we assume that the boundary layer is laminar. From Eq. (7.27), the drag coefficient is

$$C_D = \frac{1.328}{(137,000)^{1/2}} = 0.00359$$

Thus the drag on one side in the airflow is

$$D = C_{D2}^{\frac{1}{2}} \rho U^2 bL = 0.00359(\frac{1}{2})(1.23)(2.0)^2(3.0)(1.0) = 0.0265 \text{ N} \quad \text{Ans. (a)}$$

The boundary-layer thickness at the end of the plate is

$$\frac{\delta}{L} = \frac{5.0}{\text{Re}_L^{1/2}} = \frac{5.0}{(137,000)^{1/2}} = 0.0135$$

or  $\delta = 0.0135(1.0) = 0.0135 \text{ m} = 13.5 \text{ mm} \quad \text{Ans. (a)}$

We find the other two thicknesses simply by ratios:

$$\delta^* = \frac{1.721}{5.0} \delta = 4.65 \text{ mm} \quad \theta = \frac{\delta^*}{2.59} = 1.79 \text{ mm} \quad \text{Ans. (a)}$$

Notice that no conversion factors are needed with SI units.

**Part (b)** The water Reynolds number is

$$\text{Re}_L = \frac{2.0(1.0)}{1.02 \times 10^{-6}} = 1.96 \times 10^6$$

This is rather close to the critical value of  $3 \times 10^6$ , so that a rough surface or noisy free stream might trigger transition to turbulence; but let us assume that the flow is laminar. The water drag coefficient is

$$C_D = \frac{1.328}{(1.96 \times 10^6)^{1/2}} = 0.000949$$

and  $D = 0.000949(\frac{1}{2})(1000)(2.0)^2(3.0)(1.0) = 5.70 \text{ N} \quad \text{Ans. (b)}$

The drag is 215 times more for water in spite of the higher Reynolds number and lower drag coefficient because water is 57 times more viscous and 813 times denser than air. From Eq. (7.26), in laminar flow, it should have  $(57)^{1/2}(813)^{1/2} = 7.53(28.5) = 215$  times more drag.

The boundary-layer thickness is given by

$$\frac{\delta}{L} = \frac{5.0}{(1.96 \times 10^6)^{1/2}} = 0.00357$$

or  $\delta = 0.00357(1000 \text{ mm}) = 3.57 \text{ mm} \quad \text{Ans. (b)}$

By scaling down we have

$$\delta^* = \frac{1.721}{5.0} \delta = 1.23 \text{ mm} \quad \theta = \frac{\delta^*}{2.59} = 0.48 \text{ mm} \quad \text{Ans. (b)}$$

The water layer is 3.8 times thinner than the air layer, which reflects the square root of the 14.3 ratio of air to water kinematic viscosity.

## Turbulent Flow

There is no exact theory for turbulent flat-plate flow, although there are many elegant computer solutions of the boundary-layer equations using various empirical models for the turbulent eddy viscosity [9]. The most widely accepted result is simply an integral analysis similar to our study of the laminar-profile approximation (7.6).

We begin with Eq. (7.5), which is valid for laminar or turbulent flow. We write it here for convenient reference:

$$\tau_w(x) = \rho U^2 \frac{d\theta}{dx} \quad (7.32)$$

From the definition of  $c_f$ , Eq. (7.10), this can be rewritten as

$$c_f = 2 \frac{d\theta}{dx} \quad (7.33)$$

Now recall from Fig. 7.5 that the turbulent profiles are nowhere near parabolic. Going back to Fig. 6.9, we see that flat-plate flow is very nearly logarithmic, with a slight outer wake and a thin viscous sublayer. Therefore, just as in turbulent pipe flow, we assume that the logarithmic law (6.21) holds all the way across the boundary layer

$$\frac{u}{u^*} \approx \frac{1}{\kappa} \ln \frac{yu^*}{\nu} + B \quad u^* = \left( \frac{\tau_w}{\rho} \right)^{1/2} \quad (7.34)$$

with, as usual,  $\kappa = 0.41$  and  $B = 5.0$ . At the outer edge of the boundary layer,  $y = \delta$  and  $u = U$ , and Eq. (7.34) becomes

$$\frac{U}{u^*} = \frac{1}{\kappa} \ln \frac{\delta u^*}{\nu} + B \quad (7.35)$$

But the definition of the skin-friction coefficient, Eq. (7.10), is such that the following identities hold:

$$\frac{U}{u^*} \equiv \left( \frac{2}{c_f} \right)^{1/2} \quad \frac{\delta u^*}{\nu} \equiv \text{Re}_\delta \left( \frac{c_f}{2} \right)^{1/2} \quad (7.36)$$

Therefore Eq. (7.35) is a *skin-friction law* for turbulent flat-plate flow

$$\left( \frac{2}{c_f} \right)^{1/2} \approx 2.44 \ln \left[ \text{Re}_\delta \left( \frac{c_f}{2} \right)^{1/2} \right] + 5.0 \quad (7.37)$$

It is a complicated law, but we can at least solve for a few values and list them:

| $\text{Re}_\delta$ | $10^4$  | $10^5$  | $10^6$  | $10^7$  |
|--------------------|---------|---------|---------|---------|
| $c_f$              | 0.00493 | 0.00315 | 0.00217 | 0.00158 |

Following a suggestion of Prandtl, we can forget the complex log friction law (7.37) and simply fit the numbers in the table to a power-law approximation

$$c_f \approx 0.02 \operatorname{Re}_\delta^{-1/6} \quad (7.38)$$

This we shall use as the left-hand side of Eq. (7.33). For the right-hand side, we need an estimate for  $\theta(x)$  in terms of  $\delta(x)$ . If we use the logarithmic-law profile (7.34), we shall be up to our hips in logarithmic integrations for the momentum thickness. Instead we follow another suggestion of Prandtl, who pointed out that the turbulent profiles in Fig. 7.5 can be approximated by a one-seventh-power law

$$\left(\frac{u}{U}\right)_{\text{turb}} \approx \left(\frac{y}{\delta}\right)^{1/7} \quad (7.39)$$

This is shown as a dashed line in Fig. 7.5. It is an excellent fit to the low-Reynolds-number turbulent data, which were all that were available to Prandtl at the time. With this simple approximation, the momentum thickness (7.28) can easily be evaluated:

$$\theta \approx \int_0^\delta \left(\frac{y}{\delta}\right)^{1/7} \left[1 - \left(\frac{y}{\delta}\right)^{1/7}\right] dy = \frac{7}{72} \delta \quad (7.40)$$

We accept this result and substitute Eqs. (7.38) and (7.40) into Kármán's momentum law (7.33)

$$c_f = 0.02 \operatorname{Re}_\delta^{-1/6} = 2 \frac{d}{dx} \left(\frac{7}{72} \delta\right)$$

or

$$\operatorname{Re}_\delta^{-1/6} = 9.72 \frac{d\delta}{dx} = 9.72 \frac{d(\operatorname{Re}\delta)}{d(\operatorname{Re}_x)} \quad (7.41)$$

Separate the variables and integrate, assuming  $\delta = 0$  at  $x = 0$ :

$$\operatorname{Re}_\delta \approx 0.16 \operatorname{Re}_x^{6/7} \quad \text{or} \quad \frac{\delta}{x} \approx \frac{0.16}{\operatorname{Re}_x^{1/7}} \quad (7.42)$$

Thus the thickness of a turbulent boundary layer increases as  $x^{6/7}$ , far more rapidly than the laminar increase  $x^{1/2}$ . Equation (7.42) is the solution to the problem, because all other parameters are now available. For example, combining Eqs. (7.42) and (7.38), we obtain the friction variation

$$c_f \approx \frac{0.027}{\operatorname{Re}_x^{1/7}} \quad (7.43)$$

Writing this out in dimensional form, we have

$$\tau_{w,\text{turb}} \approx \frac{0.0135 \mu^{1/7} \rho^{6/7} U^{13/7}}{x^{1/7}} \quad (7.44)$$

Turbulent plate friction drops slowly with  $x$ , increases nearly as  $\rho$  and  $U^2$ , and is rather insensitive to viscosity.

We can evaluate the drag coefficient from Eq. (7.29)

$$C_D = \frac{0.031}{\operatorname{Re}_L^{1/7}} = \frac{7}{6} c_f(L) \quad (7.45)$$



Then  $C_D$  is only 16 percent greater than the trailing-edge skin friction [compare with Eq. (7.27) for laminar flow].

The displacement thickness can be estimated from the one-seventh-power law and Eq. (7.12):

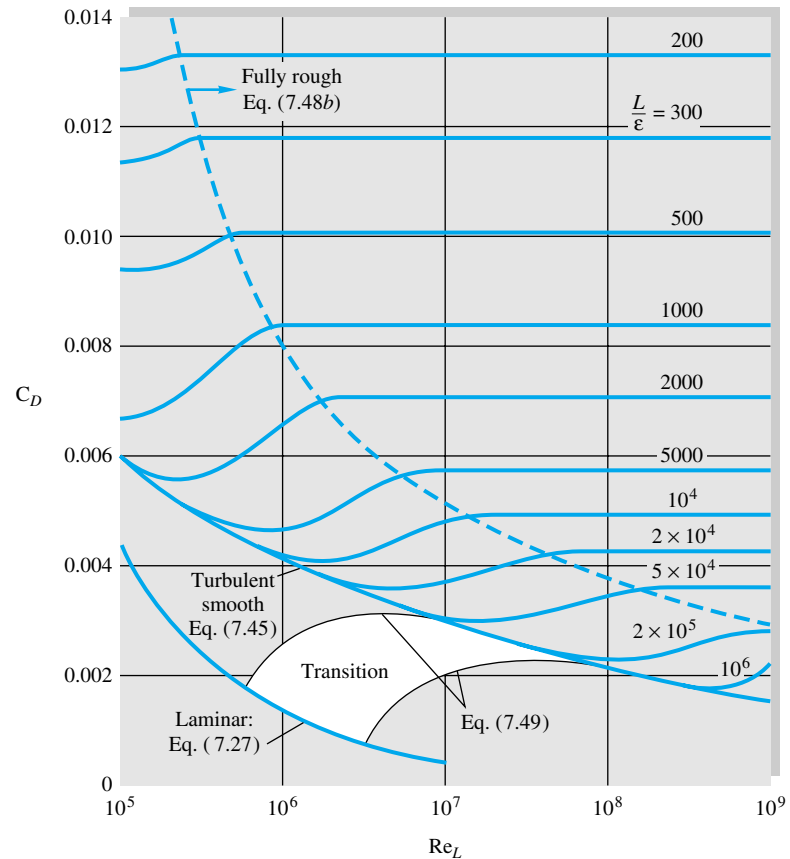
$$\delta^* \approx \int_0^\delta \left[ 1 - \left( \frac{y}{\delta} \right)^{1/7} \right] dy = \frac{1}{8} \delta \quad (7.46)$$

The turbulent flat-plate shape factor is approximately

$$H = \frac{\delta^*}{\theta} = \frac{\frac{1}{8}}{\frac{7}{72}} = 1.3 \quad (7.47)$$

These are the basic results of turbulent flat-plate theory.

Figure 7.6 shows flat-plate drag coefficients for both laminar- and turbulent-flow conditions. The smooth-wall relations (7.27) and (7.45) are shown, along with the effect of wall roughness, which is quite strong. The proper roughness parameter here is  $x/\epsilon$  or  $L/\epsilon$ , by analogy with the pipe parameter  $\epsilon/d$ . In the fully rough regime,  $C_D$  is independent of the Reynolds number, so that the drag varies exactly as  $U^2$  and is inde-



**Fig. 7.6** Drag coefficient of laminar and turbulent boundary layers on smooth and rough flat plates. This chart is the flat-plate analog of the Moody diagram of Fig. 6.13.

pendent of  $\mu$ . Reference 2 presents a theory of rough flat-plate flow, and Ref. 1 gives a curve fit for skin friction and drag in the fully rough regime:

$$c_f \approx \left( 2.87 + 1.58 \log \frac{x}{\epsilon} \right)^{-2.5} \quad (7.48a)$$

$$C_D \approx \left( 1.89 + 1.62 \log \frac{L}{\epsilon} \right)^{-2.5} \quad (7.48b)$$

Equation (7.48b) is plotted to the right of the dashed line in Fig. 7.6. The figure also shows the behavior of the drag coefficient in the transition region  $5 \times 10^5 < \text{Re}_L < 8 \times 10^7$ , where the laminar drag at the leading edge is an appreciable fraction of the total drag. Schlichting [1] suggests the following curve fits for these transition drag curves depending upon the Reynolds number  $\text{Re}_{\text{trans}}$  where transition begins:

$$C_D \approx \begin{cases} \frac{0.031}{\text{Re}_L^{1/7}} - \frac{1440}{\text{Re}_L} & \text{Re}_{\text{trans}} = 5 \times 10^5 \\ \frac{0.031}{\text{Re}_L^{1/7}} - \frac{8700}{\text{Re}_L} & \text{Re}_{\text{trans}} = 3 \times 10^6 \end{cases} \quad (7.49a)$$

$$C_D \approx \begin{cases} \frac{0.031}{\text{Re}_L^{1/7}} - \frac{8700}{\text{Re}_L} & \text{Re}_{\text{trans}} = 3 \times 10^6 \end{cases} \quad (7.49b)$$

#### EXAMPLE 7.4

A hydrofoil 1.2 ft long and 6 ft wide is placed in a water flow of 40 ft/s, with  $\rho = 1.99$  slugs/ft<sup>3</sup> and  $\nu = 0.000011$  ft<sup>2</sup>/s. (a) Estimate the boundary-layer thickness at the end of the plate. Estimate the friction drag for (b) turbulent smooth-wall flow from the leading edge, (c) laminar turbulent flow with  $\text{Re}_{\text{trans}} = 5 \times 10^5$ , and (d) turbulent rough-wall flow with  $\epsilon = 0.0004$  ft.

#### Solution

**Part (a)** The Reynolds number is

$$\text{Re}_L = \frac{UL}{\nu} = \frac{(40 \text{ ft/s})(1.2 \text{ ft})}{0.000011 \text{ ft}^2/\text{s}} = 4.36 \times 10^6$$

Thus the trailing-edge flow is certainly turbulent. The maximum boundary-layer thickness would occur for turbulent flow starting at the leading edge. From Eq. (7.42),

$$\frac{\delta(L)}{L} = \frac{0.16}{(4.36 \times 10^6)^{1/7}} = 0.018$$

or  $\delta = 0.018(1.2 \text{ ft}) = 0.0216 \text{ ft}$  Ans. (a)

This is 7.5 times thicker than a fully laminar boundary layer at the same Reynolds number.

**Part (b)** For fully turbulent smooth-wall flow, the drag coefficient on one side of the plate is, from Eq. (7.45),

$$C_D = \frac{0.031}{(4.36 \times 10^6)^{1/7}} = 0.00349$$

Then the drag on both sides of the foil is approximately

$$D = 2C_D(\frac{1}{2}\rho U^2)bL = 2(0.00349)(\frac{1}{2})(1.99)(40)^2(6.0)(1.2) = 80 \text{ lb} \quad \text{Ans. (b)}$$

**Part (c)** With a laminar leading edge and  $\text{Re}_{\text{trans}} = 5 \times 10^5$ , Eq. (7.49a) applies:

$$C_D = 0.00349 - \frac{1440}{4.36 \times 10^6} = 0.00316$$

The drag can be recomputed for this lower drag coefficient:

$$D = 2C_D(\frac{1}{2}\rho U^2)bL = 72 \text{ lbf} \quad \text{Ans. (c)}$$

**Part (d)** Finally, for the rough wall, we calculate

$$\frac{L}{\epsilon} = \frac{1.2 \text{ ft}}{0.0004 \text{ ft}} = 3000$$

From Fig. 7.6 at  $\text{Re}_L = 4.36 \times 10^6$ , this condition is just inside the fully rough regime. Equation (7.48b) applies:

$$C_D = (1.89 + 1.62 \log 3000)^{-2.5} = 0.00644$$

and the drag estimate is

$$D = 2C_D(\frac{1}{2}\rho U^2)bL = 148 \text{ lbf} \quad \text{Ans. (d)}$$

This small roughness nearly doubles the drag. It is probable that the total hydrofoil drag is still another factor of 2 larger because of trailing-edge flow-separation effects.

## 7.5 Boundary Layers with Pressure Gradient<sup>3</sup>

The flat-plate analysis of the previous section should give us a good feeling for the behavior of both laminar and turbulent boundary layers, except for one important effect: flow separation. Prandtl showed that separation like that in Fig. 7.2b is caused by excessive momentum loss near the wall in a boundary layer trying to move downstream against increasing pressure,  $dp/dx > 0$ , which is called an *adverse pressure gradient*. The opposite case of decreasing pressure,  $dp/dx < 0$ , is called a *favorable gradient*, where flow separation can never occur. In a typical immersed-body flow, e.g., Fig. 7.2b, the favorable gradient is on the front of the body and the adverse gradient is in the rear, as discussed in detail in Chap. 8.

We can explain flow separation with a geometric argument about the second derivative of velocity  $u$  at the wall. From the momentum equation (7.19b) at the wall, where  $u = v = 0$ , we obtain

$$\left. \frac{\partial \tau}{\partial y} \right|_{\text{wall}} = \mu \left. \frac{\partial^2 u}{\partial y^2} \right|_{\text{wall}} = -\rho U \frac{dU}{dx} = \frac{dp}{dx}$$

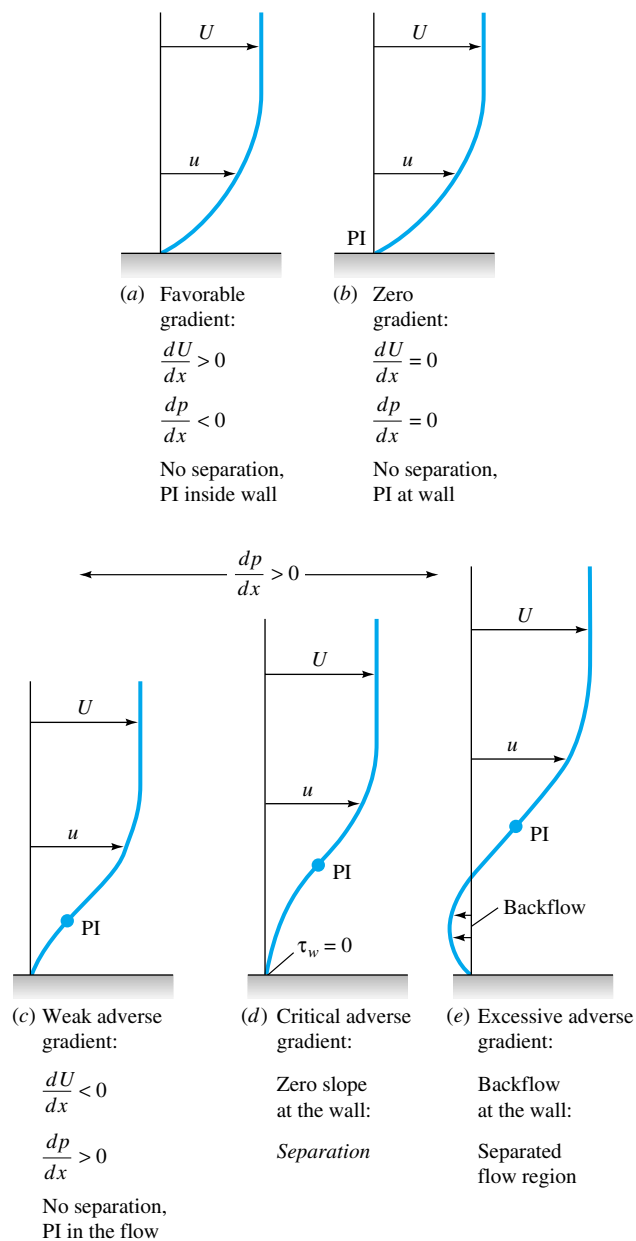
or

$$\left. \frac{\partial^2 u}{\partial y^2} \right|_{\text{wall}} = \frac{1}{\mu} \frac{dp}{dx} \quad (7.50)$$

<sup>3</sup>This section may be omitted without loss of continuity.

for either laminar or turbulent flow. Thus in an adverse gradient the second derivative of velocity is positive at the wall; yet it must be negative at the outer layer ( $y = \delta$ ) to merge smoothly with the mainstream flow  $U(x)$ . It follows that the second derivative must pass through zero somewhere in between, at a point of inflection, and any boundary-layer profile in an adverse gradient must exhibit a characteristic S shape.

Figure 7.7 illustrates the general case. In a favorable gradient (Fig. 7.7a) the profile



**Fig. 7.7** Effect of pressure gradient on boundary-layer profiles; PI = point of inflection.

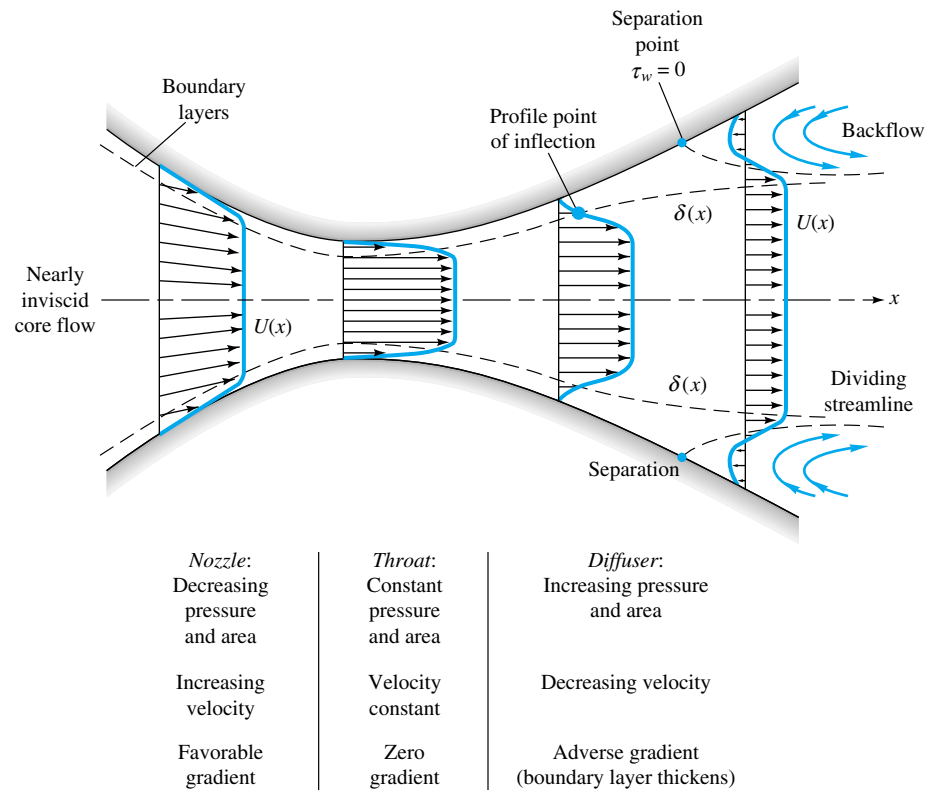
is very rounded, there is no point of inflection, there can be no separation, and laminar profiles of this type are very resistant to a transition to turbulence [1 to 3].

In a zero pressure gradient (Fig. 7.7b), e.g., flat-plate flow, the point of inflection is at the wall itself. There can be no separation, and the flow will undergo transition at  $Re_x$  no greater than about  $3 \times 10^6$ , as discussed earlier.

In an adverse gradient (Fig. 7.7c to e), a point of inflection (PI) occurs in the boundary layer, its distance from the wall increasing with the strength of the adverse gradient. For a weak gradient (Fig. 7.7c) the flow does not actually separate, but it is vulnerable to transition to turbulence at  $Re_x$  as low as  $10^5$  [1, 2]. At a moderate gradient, a critical condition (Fig. 7.7d) is reached where the wall shear is exactly zero ( $\partial u/\partial y = 0$ ). This is defined as the *separation point* ( $\tau_w = 0$ ), because any stronger gradient will actually cause backflow at the wall (Fig. 7.7e): the boundary layer thickens greatly, and the main flow breaks away, or separates, from the wall (Fig. 7.2b).

The flow profiles of Fig. 7.7 usually occur in sequence as the boundary layer progresses along the wall of a body. For example, in Fig. 7.2a, a favorable gradient occurs on the front of the body, zero pressure gradient occurs just upstream of the shoulder, and an adverse gradient occurs successively as we move around the rear of the body.

A second practical example is the flow in a duct consisting of a nozzle, throat, and diffuser, as in Fig. 7.8. The nozzle flow is a favorable gradient and never separates, nor



**Fig. 7.8** Boundary-layer growth and separation in a nozzle-diffuser configuration.

does the throat flow where the pressure gradient is approximately zero. But the expanding-area diffuser produces low velocity and increasing pressure, an adverse gradient. If the diffuser angle is too large, the adverse gradient is excessive, and the boundary layer will separate at one or both walls, with backflow, increased losses, and poor pressure recovery. In the diffuser literature [10] this condition is called *diffuser stall*, a term used also in airfoil aerodynamics (Sec. 7.6) to denote airfoil boundary-layer separation. Thus the boundary-layer behavior explains why a large-angle diffuser has heavy flow losses (Fig. 6.23) and poor performance (Fig. 6.28).

Presently boundary-layer theory can compute only up to the separation point, after which it is invalid. New techniques are now developed for analyzing the strong interaction effects caused by separated flows [5, 6].

## Laminar Integral Theory

Both laminar and turbulent theories can be developed from Kármán's general two-dimensional boundary-layer integral relation [7], which extends Eq. (7.33) to variable  $U(x)$

$$\frac{\tau_w}{\rho U^2} = \frac{1}{2} c_f = \frac{d\theta}{dx} + (2 + H) \frac{\theta}{U} \frac{dU}{dx} \quad (7.51)$$

where  $\theta(x)$  is the momentum thickness and  $H(x) = \delta^*(x)/\theta(x)$  is the shape factor. From Eq. (7.17) negative  $dU/dx$  is equivalent to positive  $dp/dx$ , that is, an adverse gradient.

We can integrate Eq. (7.51) to determine  $\theta(x)$  for a given  $U(x)$  if we correlate  $c_f$  and  $H$  with the momentum thickness. This has been done by examining typical velocity profiles of laminar and turbulent boundary-layer flows for various pressure gradients. Some examples are given in Fig. 7.9, showing that the shape factor  $H$  is a good indicator of the pressure gradient. The higher the  $H$ , the stronger the adverse gradient, and separation occurs approximately at

$$H \approx \begin{cases} 3.5 & \text{laminar flow} \\ 2.4 & \text{turbulent flow} \end{cases} \quad (7.52)$$

The laminar profiles (Fig. 7.9a) clearly exhibit the S shape and a point of inflection with an adverse gradient. But in the turbulent profiles (Fig. 7.9b) the points of inflection are typically buried deep within the thin viscous sublayer, which can hardly be seen on the scale of the figure.

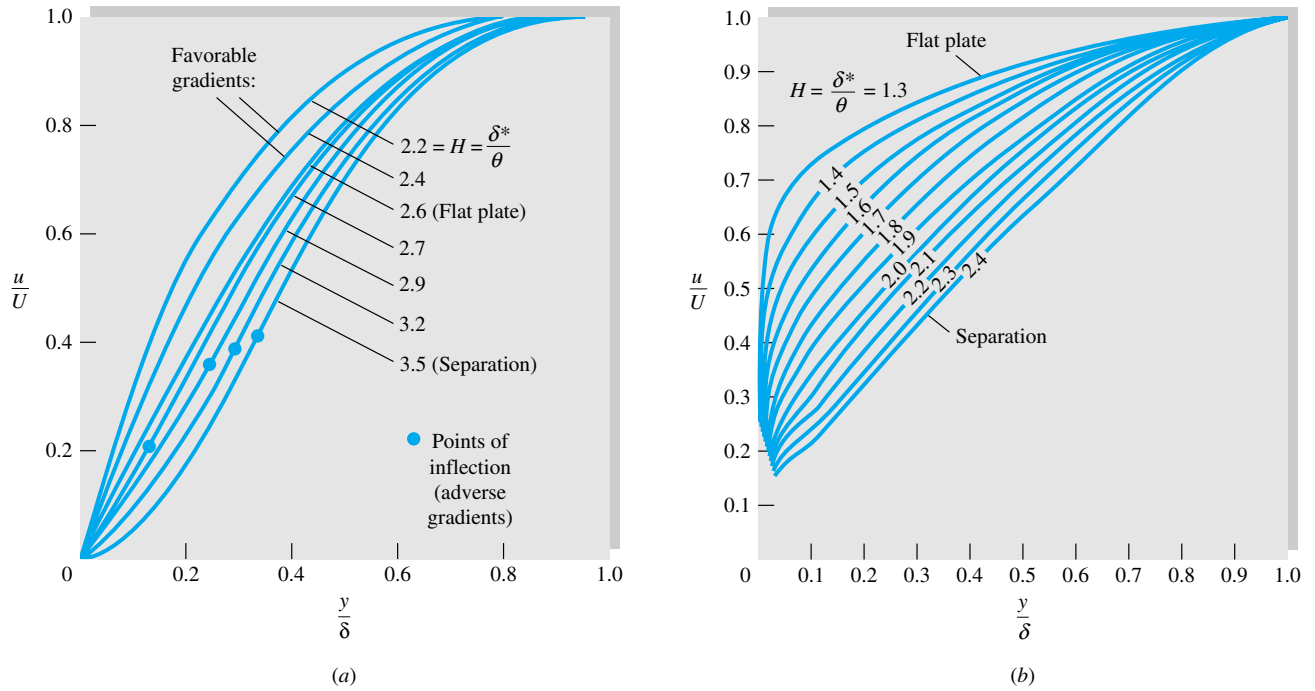
There are scores of turbulent theories in the literature, but they are all complicated algebraically and will be omitted here. The reader is referred to advanced texts [1, 2, 9].

For laminar flow, a simple and effective method was developed by Thwaites [11], who found that Eq. (7.51) can be correlated by a single dimensionless momentum-thickness variable  $\lambda$ , defined as

$$\lambda = \frac{\theta^2}{\nu} \frac{dU}{dx} \quad (7.53)$$

Using a straight-line fit to his correlation, Thwaites was able to integrate Eq. (7.51) in closed form, with the result

$$\theta^2 = \theta_0^2 \left( \frac{U_0}{U} \right)^6 + \frac{0.45\nu}{U^6} \int_0^x U^5 dx \quad (7.54)$$



**Fig. 7.9** Velocity profiles with pressure gradient: (a) laminar flow; (b) turbulent flow with adverse gradients.

where  $\theta_0$  is the momentum thickness at  $x = 0$  (usually taken to be zero). Separation ( $c_f = 0$ ) was found to occur at a particular value of  $\lambda$

$$\text{Separation:} \quad \lambda = -0.09 \quad (7.55)$$

Finally, Thwaites correlated values of the dimensionless shear stress  $S = \tau_w \theta / (\mu U)$  with  $\lambda$ , and his graphed result can be curve-fitted as follows:

$$S(\lambda) = \frac{\tau_w \theta}{\mu U} \approx (\lambda + 0.09)^{0.62} \quad (7.56)$$

This parameter is related to the skin friction by the identity

$$S \equiv \frac{1}{2} c_f \text{Re}_\theta \quad (7.57)$$

Equations (7.54) to (7.56) constitute a complete theory for the laminar boundary layer with variable  $U(x)$ , with an accuracy of  $\pm 10$  percent compared with exact digital-computer solutions of the laminar-boundary-layer equations (7.19). Complete details of Thwaites' and other laminar theories are given in Refs. 2 and 3.

As a demonstration of Thwaites' method, take a flat plate, where  $U = \text{constant}$ ,  $\lambda = 0$ , and  $\theta_0 = 0$ . Equation (7.54) integrates to

$$\theta^2 = \frac{0.45 \nu x}{U}$$

$$\text{or} \quad \frac{\theta}{x} = \frac{0.671}{\text{Re}_x^{1/2}} \quad (7.58)$$

This is within 1 percent of Blasius' exact solution, Eq. (7.30).

With  $\lambda = 0$ , Eq. (7.56) predicts the flat-plate shear to be

$$\frac{\tau_w \theta}{\mu U} = (0.09)^{0.62} = 0.225$$

$$\text{or} \quad c_f = \frac{2\tau_w}{\rho U^2} = \frac{0.671}{\text{Re}_x^{1/2}} \quad (7.59)$$

This is also within 1 percent of the Blasius result, Eq. (7.25). However, the general accuracy of this method is poorer than 1 percent because Thwaites actually "tuned" his correlation constants to make them agree with exact flat-plate theory.

We shall not compute any more boundary-layer details here, but as we go along, investigating various immersed-body flows, especially in Chap. 8, we shall use Thwaites' method to make qualitative assessments of the boundary-layer behavior.

---

### EXAMPLE 7.5

---

In 1938 Howarth proposed a linearly decelerating external-velocity distribution

$$U(x) = U_0 \left(1 - \frac{x}{L}\right) \quad (1)$$

as a theoretical model for laminar-boundary-layer study. (a) Use Thwaites' method to compute the separation point  $x_{\text{sep}}$  for  $\theta_0 = 0$ , and compare with the exact digital-computer solution  $x_{\text{sep}}/L = 0.119863$  given by H. Wipperman in 1966. (b) Also compute the value of  $c_f = 2\tau_w/(\rho U^2)$  at  $x/L = 0.1$ .

---

### Solution

---

**Part (a)** First note that  $dU/dx = -U_0/L = \text{constant}$ : Velocity decreases, pressure increases, and the pressure gradient is adverse throughout. Now integrate Eq. (7.54)

$$\theta^2 = \frac{0.45\nu}{U_0^6(1-x/L)^6} \int_0^x U_0^5 \left(1 - \frac{x}{L}\right)^5 dx = 0.075 \frac{\nu L}{U_0} \left[ \left(1 - \frac{x}{L}\right)^{-6} - 1 \right] \quad (2)$$

Then the dimensionless factor  $\lambda$  is given by

$$\lambda = \frac{\theta^2}{\nu} \frac{dU}{dx} = -\frac{\theta^2 U_0}{\nu L} = -0.075 \left[ \left(1 - \frac{x}{L}\right)^{-6} - 1 \right] \quad (3)$$

From Eq. (7.55) we set this equal to  $-0.09$  for separation

$$\lambda_{\text{sep}} = -0.09 = -0.075 \left[ \left(1 - \frac{x_{\text{sep}}}{L}\right)^{-6} - 1 \right]$$

$$\text{or} \quad \frac{x_{\text{sep}}}{L} = 1 - (2.2)^{-1/6} = 0.123 \quad \text{Ans. (a)}$$



This is less than 3 percent higher than Wipperman's exact solution, and the computational effort is very modest.

**Part (b)** To compute  $c_f$  at  $x/L = 0.1$  (just before separation), we first compute  $\lambda$  at this point, using Eq. (3)

$$\lambda(x = 0.1L) = -0.075[(1 - 0.1)^{-6} - 1] = -0.0661$$

Then from Eq. (7.56) the shear parameter is

$$S(x = 0.1L) = (-0.0661 + 0.09)^{0.62} = 0.099 = \frac{1}{2}c_f \text{Re}_\theta \quad (4)$$

We can compute  $\text{Re}_\theta$  in terms of  $\text{Re}_L$  from Eq. (2) or (3)

$$\frac{\theta^2}{L^2} = \frac{0.0661}{UL/\nu} = \frac{0.0661}{\text{Re}_L}$$

$$\text{or} \quad \text{Re}_\theta = 0.257 \text{Re}_L^{1/2} \quad \text{at} \quad \frac{x}{L} = 0.1$$

Substitute into Eq. (4):

$$0.099 = \frac{1}{2}c_f(0.257 \text{Re}_L^{1/2})$$

$$\text{or} \quad c_f = \frac{0.77}{\text{Re}_L^{1/2}} \quad \text{Re}_L = \frac{UL}{\nu} \quad \text{Ans. (b)}$$

We cannot actually compute  $c_f$  without the value of, say,  $U_0L/\nu$ .

## 7.6 Experimental External Flows

Boundary-layer theory is very interesting and illuminating and gives us a great qualitative grasp of viscous-flow behavior, but, because of flow separation, the theory does not generally allow a quantitative computation of the complete flow field. In particular, there is at present no satisfactory theory for the forces on an arbitrary body immersed in a stream flowing at an arbitrary Reynolds number. Therefore experimentation is the key to treating external flows.

Literally thousands of papers in the literature report experimental data on specific external viscous flows. This section gives a brief description of the following external-flow problems:

1. Drag of two-and three-dimensional bodies
  - a. Blunt bodies
  - b. Streamlined shapes
2. Performance of lifting bodies
  - a. Airfoils and aircraft
  - b. Projectiles and finned bodies
  - c. Birds and insects

For further reading see the goldmine of data compiled in Hoerner [12]. In later chapters we shall study data on supersonic airfoils (Chap. 9), open-channel friction (Chap. 10), and turbomachinery performance (Chap. 11).

## Drag of Immersed Bodies

Any body of any shape when immersed in a fluid stream will experience forces and moments from the flow. If the body has arbitrary shape and orientation, the flow will exert forces and moments about all three coordinate axes, as shown in Fig. 7.10. It is customary to choose one axis parallel to the free stream and positive downstream. The force on the body along this axis is called *drag*, and the moment about that axis the *rolling moment*. The drag is essentially a flow loss and must be overcome if the body is to move against the stream.

A second and very important force is perpendicular to the drag and usually performs a useful job, such as bearing the weight of the body. It is called the *lift*. The moment about the lift axis is called *yaw*.

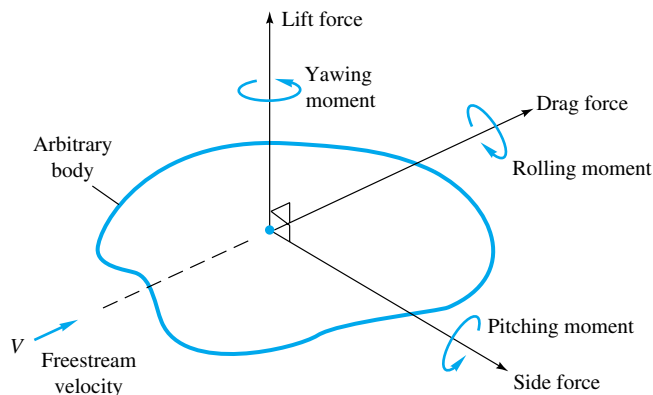
The third component, neither a loss nor a gain, is the *side force*, and about this axis is the *pitching moment*. To deal with this three-dimensional force-moment situation is more properly the role of a textbook on aerodynamics [for example, 13]. We shall limit the discussion here to lift and drag.

When the body has symmetry about the lift-drag axis, e.g., airplanes, ships, and cars moving directly into a stream, the side force, yaw, and roll vanish, and the problem reduces to a two-dimensional case: two forces, lift and drag, and one moment, pitch.

A final simplification often occurs when the body has two planes of symmetry, as in Fig. 7.11. A wide variety of shapes such as cylinders, wings, and all bodies of revolution satisfy this requirement. If the free stream is parallel to the intersection of these two planes, called the *principal chord line of the body*, the body experiences drag only, with no lift, side force, or moments.<sup>4</sup> This type of degenerate one-force drag data is what is most commonly reported in the literature, but if the free stream is not parallel to the chord line, the body will have an unsymmetric orientation and all three forces and three moments can arise in principle.

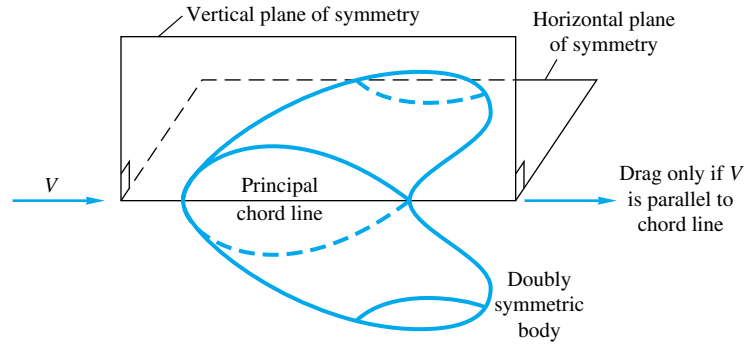
In low-speed flow past geometrically similar bodies with identical orientation and relative roughness, the drag coefficient should be a function of the body Reynolds number

$$C_D = f(\text{Re}) \quad (7.60)$$



**Fig. 7.10** Definition of forces and moments on a body immersed in a uniform flow.

<sup>4</sup>In bodies with shed vortices, such as the cylinder in Fig. 5.2, there may be *oscillating* lift, side force, and moments, but their mean value is zero.



**Fig. 7.11** Only the drag force occurs if the flow is parallel to both planes of symmetry.

The Reynolds number is based upon the free-stream velocity  $V$  and a characteristic length  $L$  of the body, usually the chord or body length parallel to the stream

$$\text{Re} = \frac{VL}{\nu} \quad (7.61)$$

For cylinders, spheres, and disks, the characteristic length is the diameter  $D$ .

### Characteristic Area

Drag coefficients are defined by using a characteristic area  $A$  which may differ depending upon the body shape:

$$C_D = \frac{\text{drag}}{\frac{1}{2}\rho V^2 A} \quad (7.62)$$

The factor  $\frac{1}{2}$  is our traditional tribute to Euler and Bernoulli. The area  $A$  is usually one of three types:

1. *Frontal area*, the body as seen from the stream; suitable for thick, stubby bodies, such as spheres, cylinders, cars, missiles, projectiles, and torpedoes.
2. *Planform area*, the body area as seen from above; suitable for wide, flat bodies such as wings and hydrofoils.
3. *Wetted area*, customary for surface ships and barges.

In using drag or other fluid-force data, it is important to note what length and area are being used to scale the measured coefficients.

### Friction Drag and Pressure Drag

As we have mentioned, the theory of drag is weak and inadequate, except for the flat plate. This is because of flow separation. Boundary-layer theory can predict the separation point but cannot accurately estimate the (usually low) pressure distribution in the separated region. The difference between the high pressure in the front stagnation region and the low pressure in the rear separated region causes a large drag contribution called *pressure drag*. This is added to the integrated shear stress or *friction drag* of the body, which it often exceeds:

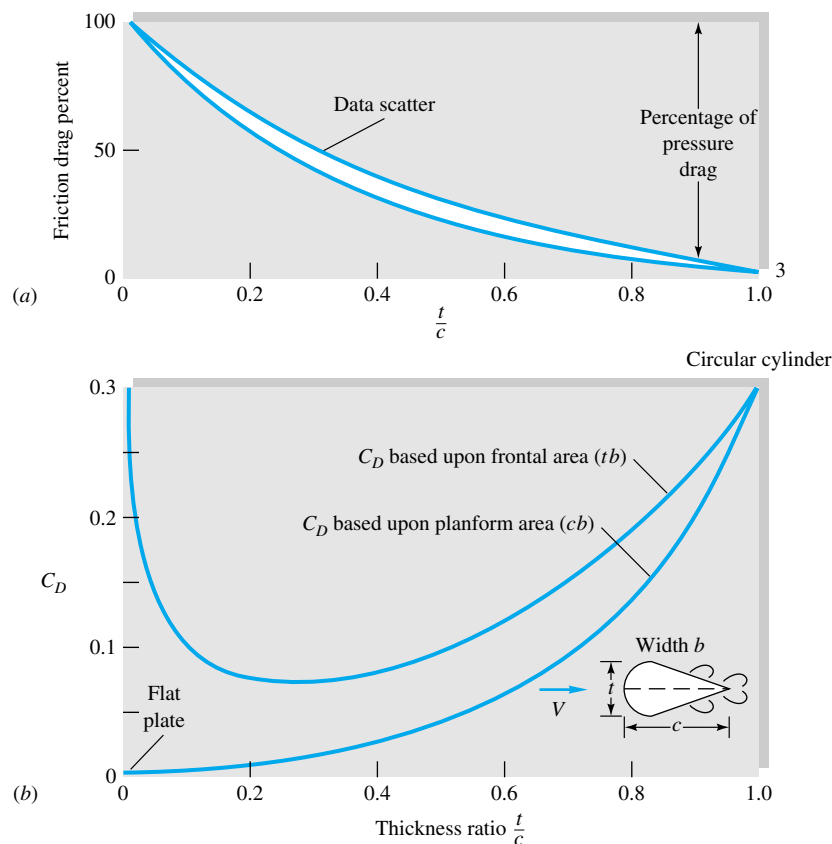
$$C_D = C_{D,\text{press}} + C_{D,\text{fric}} \quad (7.63)$$

The relative contribution of friction and pressure drag depends upon the body's shape, especially its thickness. Figure 7.12 shows drag data for a streamlined cylinder of very large depth into the paper. At zero thickness the body is a flat plate and exhibits 100 percent friction drag. At thickness equal to the chord length, simulating a circular cylinder, the friction drag is only about 3 percent. Friction and pressure drag are about equal at thickness  $t/c = 0.25$ . Note that  $C_D$  in Fig. 7.12b looks quite different when based upon frontal area instead of planform area, planform being the usual choice for this body shape. The two curves in Fig. 7.12b represent exactly the same drag data.

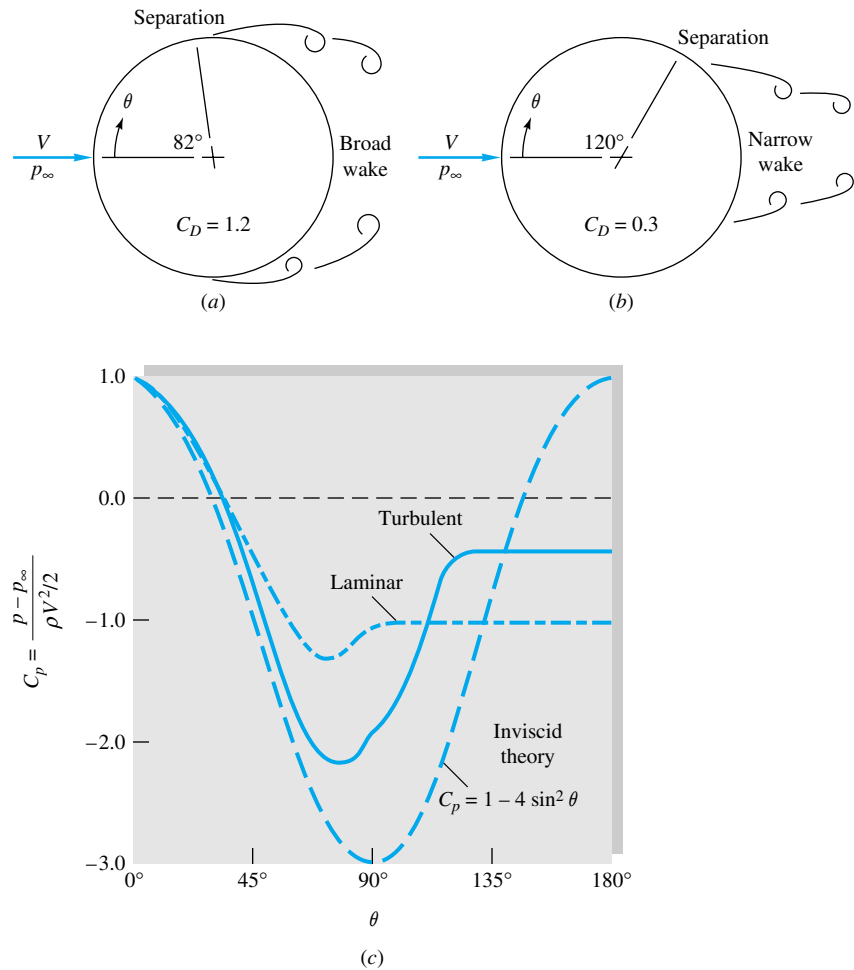
Figure 7.13 illustrates the dramatic effect of separated flow and the subsequent failure of boundary-layer theory. The theoretical inviscid pressure distribution on a circular cylinder (Chap. 8) is shown as the dashed line in Fig. 7.13c:

$$C_p = \frac{p - p_\infty}{\frac{1}{2}\rho V^2} = 1 - 4 \sin^2 \theta \quad (7.64)$$

where  $p_\infty$  and  $V$  are the pressure and velocity, respectively, in the free stream. The actual laminar and turbulent boundary-layer pressure distributions in Fig. 7.13c are startlingly different from those predicted by theory. Laminar flow is very vulnerable to the adverse gradient on the rear of the cylinder, and separation occurs at  $\theta = 82^\circ$ , which



**Fig. 7.12** Drag of a streamlined two-dimensional cylinder at  $Re_c = 10^6$ : (a) effect of thickness ratio on percentage of friction drag; (b) total drag versus thickness when based upon two different areas.



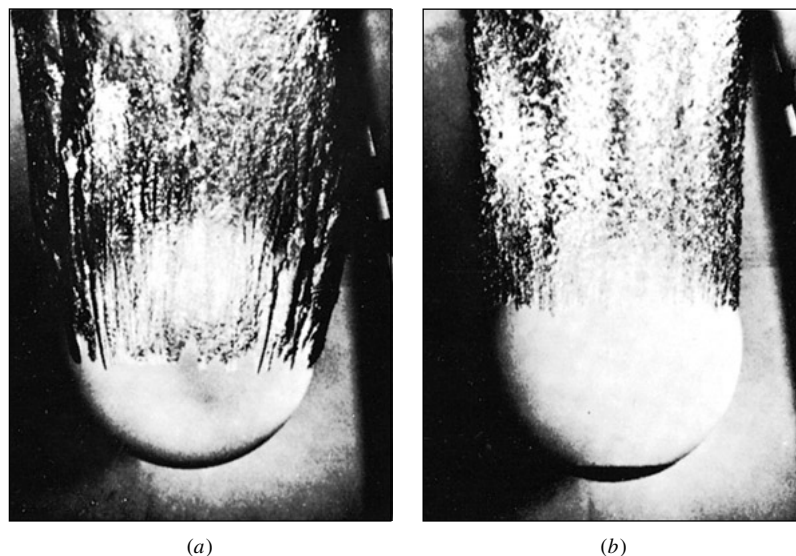
**Fig. 7.13** Flow past a circular cylinder: (a) laminar separation; (b) turbulent separation; (c) theoretical and actual surface-pressure distributions.

certainly could not have been predicted from inviscid theory. The broad wake and very low pressure in the separated laminar region cause the large drag  $C_D = 1.2$ .

The turbulent boundary layer in Fig. 7.13b is more resistant, and separation is delayed until  $\theta = 120^\circ$ , with a resulting smaller wake, higher pressure on the rear, and 75 percent less drag,  $C_D = 0.3$ . This explains the sharp drop in drag at transition in Fig. 5.3.

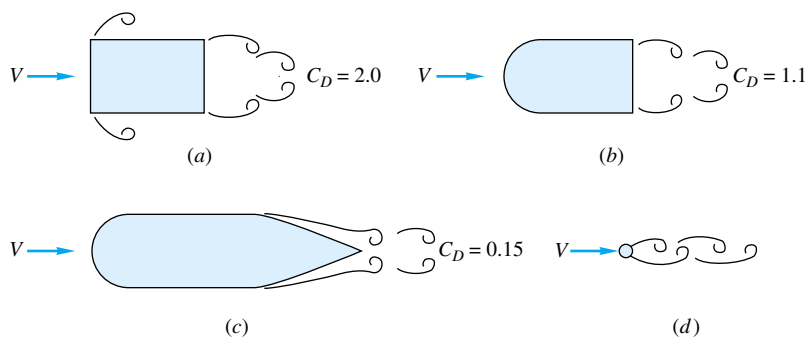
The same sharp difference between vulnerable laminar separation and resistant turbulent separation can be seen for a sphere in Fig. 7.14. The laminar flow (Fig. 7.14a) separates at about  $80^\circ$ ,  $C_D = 0.5$ , while the turbulent flow (Fig. 7.14b) separates at  $120^\circ$ ,  $C_D = 0.2$ . Here the Reynolds numbers are exactly the same, and the turbulent boundary layer is induced by a patch of sand roughness at the nose of the ball. Golf balls fly in this range of Reynolds numbers, which is why they are deliberately dimpled – to induce a turbulent boundary layer and lower drag. Again we would find the actual pressure distribution on the sphere to be quite different from that predicted by inviscid theory.

**Fig. 7.14** Strong differences in laminar and turbulent separation on an 8.5-in bowling ball entering water at 25 ft/s: (a) smooth ball, laminar boundary layer; (b) same entry, turbulent flow induced by patch of nose-sand roughness. (U.S. Navy photograph, Ordnance Test Station, Pasadena Annex.)



In general, we cannot overstate the importance of body streamlining to reduce drag at Reynolds numbers above about 100. This is illustrated in Fig. 7.15. The rectangular cylinder (Fig. 7.15a) has rampant separation at all sharp corners and very high drag. Rounding its nose (Fig. 7.15b) reduces drag by about 45 percent, but  $C_D$  is still high. Streamlining its rear to a sharp trailing edge (Fig. 7.15c) reduces its drag another 85 percent to a practical minimum for the given thickness. As a dramatic contrast, the circular cylinder (Fig. 7.15d) has one-eighth the thickness and one-three-hundredth the cross section (c) (Fig. 7.15c), yet it has the same drag. For high-performance vehicles and other moving bodies, the name of the game is drag reduction, for which intense research continues for both aerodynamic and hydrodynamic applications [20, 39].

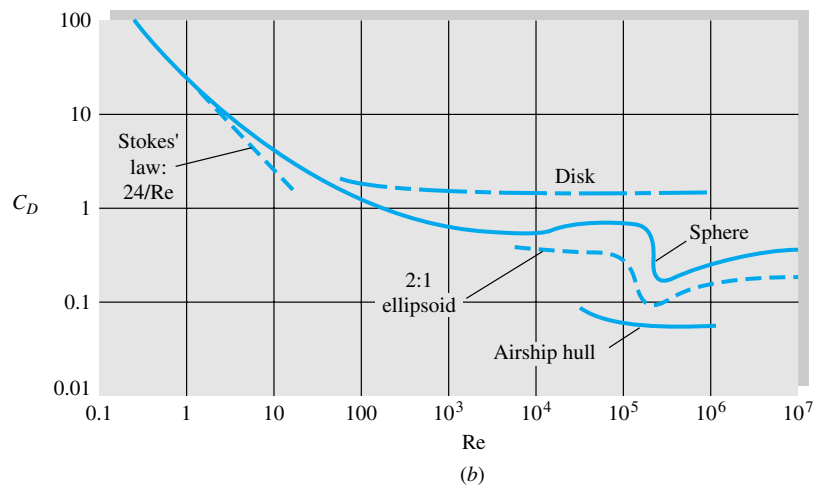
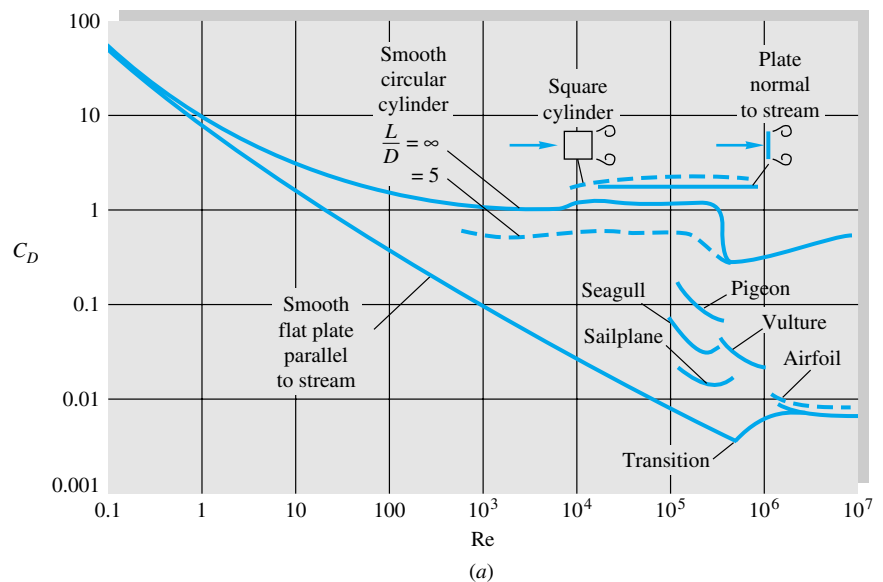
The drag of some representative wide-span (nearly two-dimensional) bodies is shown versus the Reynolds number in Fig. 7.16a. All bodies have high  $C_D$  at very low (*creeping flow*)  $Re \leq 1.0$ , while they spread apart at high Reynolds numbers according to



**Fig. 7.15** The importance of streamlining in reducing drag of a body ( $C_D$  based on frontal area): (a) rectangular cylinder; (b) rounded nose; (c) rounded nose and streamlined sharp trailing edge; (d) circular cylinder with the same drag as case (c).




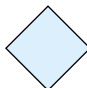

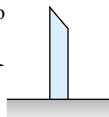

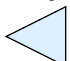

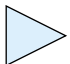

their degree of streamlining. All values of  $C_D$  are based on the planform area except the plate normal to the flow. The birds and the sailplane are, of course, not very two-dimensional, having only modest span length. Note that birds are not nearly as efficient as modern sailplanes or airfoils [14, 15].

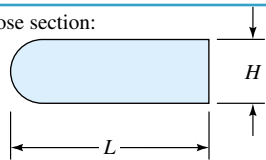

Table 7.2 gives a few data on drag, based on frontal area, of two-dimensional bodies of various cross section, at  $Re \geq 10^4$ . The sharp-edged bodies, which tend to cause flow separation regardless of the character of the boundary layer, are insensitive to the Reynolds number. The elliptic cylinders, being smoothly rounded, have the laminar-to-turbulent transition effect of Figs. 7.13 and 7.14 and are therefore quite sensitive to whether the boundary layer is laminar or turbulent.

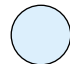





**Fig. 7.16** Drag coefficients of smooth bodies at low Mach numbers: (a) two-dimensional bodies; (b) three-dimensional bodies. Note the Reynolds-number independence of blunt bodies at high  $Re$ .

**Table 7.2** Drag of Two-Dimensional Bodies at  $Re \geq 10^4$

| Shape   | $C_D$ based on frontal area | Shape   | $C_D$ based on frontal area | Shape   | $C_D$ based on frontal area |
|---|-----------------------------|---|-----------------------------|---|-----------------------------|
| Square cylinder:  |                             | Half-cylinder:  |                             | Plate:  |                             |
|  | 2.1                         |  | 1.2                         |  | 2.0                         |
|  | 1.6                         |  | 1.7                         | Thin plate normal to a wall:  |                             |
| Half tube:  |                             | Equilateral triangle:   |                             |  | 1.4                         |
|  | 1.2                         |  | 1.6                         |   |                             |
|  | 2.3                         |  | 2.0                         | Hexagon:  |                             |
|   |                             |   |                             |  | 1.0 $\uparrow$ 0.7          |

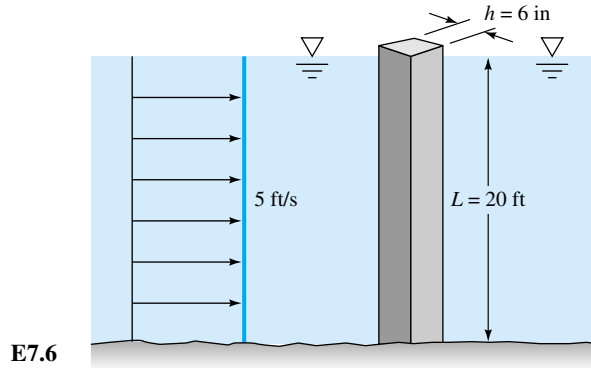
| Shape  | $C_D$ based on frontal area |      |      |      |      |      |     |     |     |
|--|-----------------------------|------|------|------|------|------|-----|-----|-----|
| Rounded nose section:  |                             |      |      |      |      |      |     |     |     |
|   | $L/H:$                      | 0.5  | 1.0  | 2.0  | 4.0  | 6.0  |     |     |     |
|  | $C_D:$                      | 1.16 | 0.90 | 0.70 | 0.68 | 0.64 |     |     |     |
| Flat nose section  |                             |      |      |      |      |      |     |     |     |
|  | $L/H:$                      | 0.1  | 0.4  | 0.7  | 1.2  | 2.0  | 2.5 | 3.0 | 6.0 |
|  | $C_D:$                      | 1.9  | 2.3  | 2.7  | 2.1  | 1.8  | 1.4 | 1.3 | 0.9 |

| Elliptical cylinder: |   | Laminar | Turbulent |
|----------------------|---|---------|-----------|
| 1:1                  |  | 1.2     | 0.3       |
| 2:1                  |  | 0.6     | 0.2       |
| 4:1                  |  | 0.35    | 0.15      |
| 8:1                  |  | 0.25    | 0.1       |



**EXAMPLE 7.6**

A square 6-in piling is acted on by a water flow of 5 ft/s that is 20 ft deep, as shown in Fig. E7.6. Estimate the maximum bending exerted by the flow on the bottom of the piling.

**Solution**

Assume seawater with  $\rho = 1.99$  slugs/ft<sup>3</sup> and kinematic viscosity  $\nu = 0.000011$  ft<sup>2</sup>/s. With a piling width of 0.5 ft, we have

$$\text{Re}_h = \frac{(5 \text{ ft/s})(0.5 \text{ ft})}{0.000011 \text{ ft}^2/\text{s}} = 2.3 \times 10^5$$

This is the range where Table 7.2 applies. The worst case occurs when the flow strikes the flat side of the piling,  $C_D \approx 2.1$ . The frontal area is  $A = Lh = (20 \text{ ft})(0.5 \text{ ft}) = 10 \text{ ft}^2$ . The drag is estimated by

$$F = C_D \left( \frac{1}{2} \rho V^2 A \right) \approx 2.1 \left( \frac{1}{2} \right) (1.99 \text{ slugs/ft}^3) (5 \text{ ft/s})^2 (10 \text{ ft}^2) = 522 \text{ lbf}$$

If the flow is uniform, the center of this force should be at approximately middepth. Therefore the bottom bending moment is

$$M_0 \approx \frac{FL}{2} = 522(10) = 5220 \text{ ft} \cdot \text{lbf} \quad \text{Ans.}$$


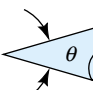
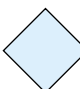



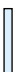

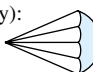


According to the flexure formula from strength of materials, the bending stress at the bottom would be

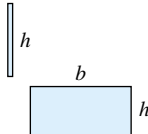

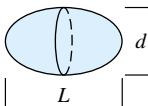
$$S = \frac{M_0 y}{I} = \frac{(5220 \text{ ft} \cdot \text{lb})(0.25 \text{ ft})}{\frac{1}{12} (0.5 \text{ ft})^4} = 251,000 \text{ lbf/ft}^2 = 1740 \text{ lbf/in}^2$$

to be multiplied, of course, by the stress-concentration factor due to the built-in end conditions.

Some drag coefficients of three-dimensional bodies are listed in Table 7.3 and Fig. 7.16*b*. Again we can conclude that sharp edges always cause flow separation and high drag which is insensitive to the Reynolds number. Rounded bodies like the ellipsoid have drag which depends upon the point of separation, so that both the Reynolds num-

**Table 7.3** Drag of Three-Dimensional Bodies at  $Re \geq 10^4$

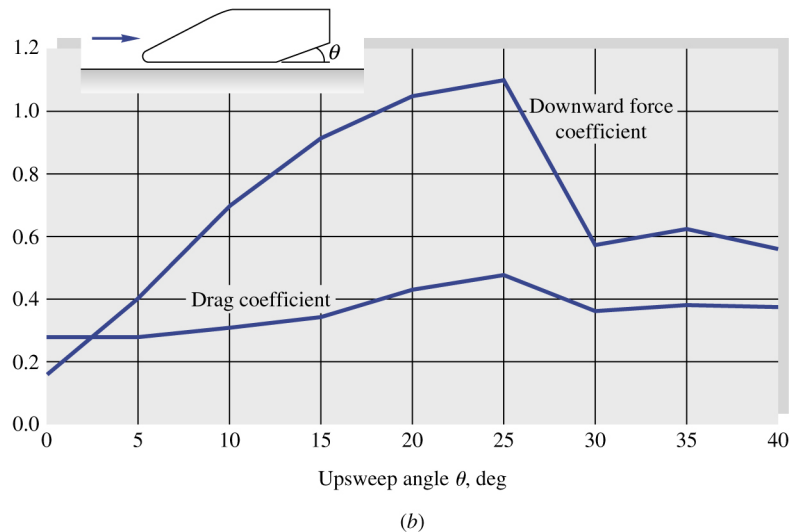
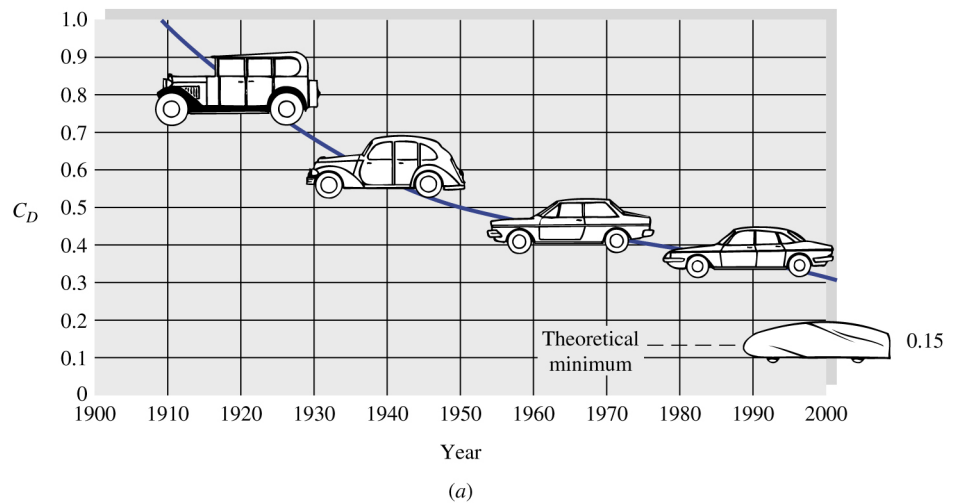
| Body   | $C_D$ based on frontal area | Body   | $C_D$ based on frontal area  |               |               |               |               |      |      |      |          |
|--|-----------------------------|--|--|---------------|---------------|---------------|---------------|------|------|------|----------|
| Cube:<br>                     | 1.07                        | Cone:<br>                         | $\theta$ :   | 10°           | 20°           | 30°           | 40°           | 60°  | 75°  | 90°  |          |
|                               | 0.81                        |  | $C_D$ :  | 0.30          | 0.40          | 0.55          | 0.65          | 0.80 | 1.05 | 1.15 |          |
| Cup:<br>                      | 1.4                         | Short cylinder, laminar flow:<br> | $L/D$ :  | 1             | 2             | 3             | 5             | 10   | 20   | 40   | $\infty$ |
|                               | 0.4                         |  | $C_D$ :  | 0.64          | 0.68          | 0.72          | 0.74          | 0.82 | 0.91 | 0.98 | 1.20     |
| Disk:<br>                     | 1.17                        | Porous parabolic dish [23]:<br>   | Porosity:  | 0             | 0.1           | 0.2           | 0.3           | 0.4  | 0.5  |      |          |
| Parachute (Low porosity):<br> | 1.2                         |  | $\leftarrow C_D$ :   | 1.42          | 1.33          | 1.20          | 1.05          | 0.95 | 0.82 |      |          |
|  |                             |  | $\rightarrow C_D$ :  | 0.95          | 0.92          | 0.90          | 0.86          | 0.83 | 0.80 |      |          |
|  |                             | Average person:<br>               | $C_D A \approx 9 \text{ ft}^2 \quad \uparrow \quad C_D A \approx 1.2 \text{ ft}^2$ |               |               |               |               |      |      |      |          |
|  |                             | Pine and spruce trees [24]:<br>   | $U, \text{ m/s}$ :   | 10            | 20            | 30            | 40            |      |      |      |          |
|  |                             |  | $C_D$ :  | $1.2 \pm 0.2$ | $1.0 \pm 0.2$ | $0.7 \pm 0.2$ | $0.5 \pm 0.2$ |      |      |      |          |

| Body  | Ratio    | $C_D$ based on frontal area | Body  | Ratio | $C_D$ based on frontal area |
|---|----------|-----------------------------|---|-------|-----------------------------|
| Rectangular plate:<br> | $b/h$    |                             | Flat-faced cylinder:<br> | $L/d$ |                             |
|   | 1        | 1.18                        |   | 0.5   | 1.15                        |
|   | 5        | 1.2                         |   | 1     | 0.90                        |
|   | 10       | 1.3                         |   | 2     | 0.85                        |
|   | 20       | 1.5                         |   | 4     | 0.87                        |
|   | $\infty$ | 2.0                         |   | 8     | 0.99                        |
| Ellipsoid:<br>         | $L/d$    |                             |   |       |                             |
|   | 0.75     |                             |   |       |                             |
|   | 1        | 0.5                         |   |       | 0.2                         |
|   | 2        | 0.47                        |   |       | 0.2                         |
|   | 4        | 0.27                        |   |       | 0.13                        |
|   | 8        | 0.25                        |   |       | 0.1                         |
|   |          | 0.2                         |   |       | 0.08                        |

ber and the character of the boundary layer are important. Body length will generally decrease pressure drag by making the body relatively more slender, but sooner or later the friction drag will catch up. For the flat-faced cylinder in Table 7.3, pressure drag decreases with  $L/d$  but friction increases, so that minimum drag occurs at about  $L/d = 2$ .

### Aerodynamic Forces on Road Vehicles

Automobiles and trucks are now the subject of much research on aerodynamic forces, both lift and drag [21]. At least one textbook is devoted to the subject [22]. Consumer, manufacturer, and government interest has cycled between high speed/high horsepower and lower speed/lower drag. Better streamlining of car shapes has resulted over the years in a large decrease in the automobile drag coefficient, as shown in Fig. 7.17a. Modern cars have an average drag coefficient of about 0.35, based upon the frontal



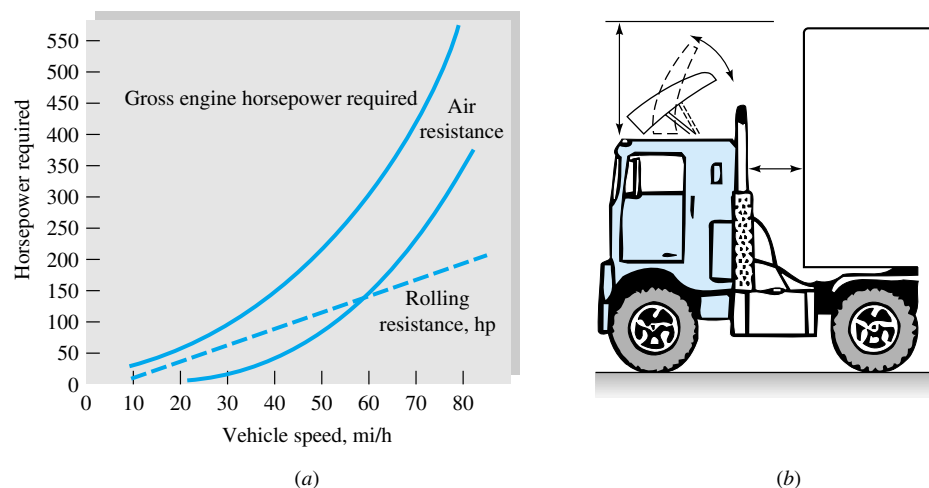
**Fig. 7.17** Aerodynamics of automobiles: (a) the historical trend for drag coefficients [From Ref. 21]; (b) effect of bottom rear upsweep angle on drag and downward lift force [From Ref. 25].

area. Since the frontal area has also decreased sharply, the actual raw drag *force* on cars has dropped even more than indicated in Fig. 7.17*a*. The practical minimum, shown tentatively for the year 2000, is  $C_D \approx 0.15$  for a tear-shaped vehicle, which can be achieved any time the public is willing to purchase such a shape. Note that basing  $C_D$  on the frontal area is awkward, since one would need an accurate drawing of the automobile to estimate its frontal area. For this reason, some technical articles simply report the raw drag in newtons or pound-force, or the product  $C_D A$ .

Many companies and laboratories have automotive wind tunnels, some full-scale and/or with moving floors to approximate actual kinematic similarity. The blunt shapes of most automobiles, together with their proximity to the ground, cause a wide variety of flow and geometric effects. Simple changes in part of the shape can have a large influence on aerodynamic forces. Figure 7.17*b* shows force data by Bearman et al. [25] for an idealized smooth automobile shape with upsweep in the rear of the bottom section. We see that by simply adding an upsweep angle of  $25^\circ$ , we can quadruple the downward force, gaining tire traction at the expense of doubling the drag. For this study, the effect of a moving floor was small—about a 10 percent increase in both drag and lift compared to a fixed floor.

It is difficult to quantify the exact effect of geometric changes on automotive forces, since, e.g., changes in a windshield shape might interact with downstream flow over the roof and trunk. Nevertheless, based on correlation of many model and full-scale tests, Ref. 26 proposes a formula for automobile drag which adds separate effects such as front ends, cowls, fenders, windshield, roofs, and rear ends.

Figure 7.18 shows the horsepower required to drive a typical tractor-trailer truck at speeds up to 80 mi/h (117 ft/s or 36 m/s). The rolling resistance increases linearly and the air drag quadratically with speed ( $C_D \approx 1.0$ ). The two are about equally important at 55 mi/h, which is the nominal speed limit in the United States. As shown in Fig. 7.18*b*, air drag can be reduced by attaching a deflector to the top of the tractor. If the angle of the deflector is adjusted to carry the flow smoothly over the top and around the sides of the trailer, the reduction in  $C_D$  is about 20 percent. Thus, at 55 mi/h the total resistance is reduced 10 percent, with a corresponding reduction in

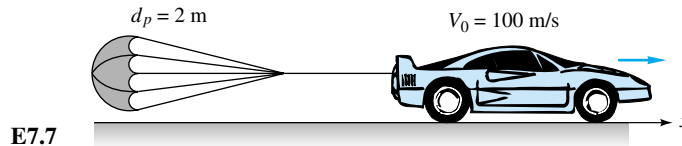


**Fig. 7.18** Drag reduction of a tractor-trailer truck: (a) horsepower required to overcome resistance; (b) deflector added to cab reduces air drag by 20 percent. (*Uniroyal Inc.*)

fuel costs and/or trip time for the trucker. This type of applied fluids engineering can be a large factor in many of the conservation-oriented transportation problems of the future.

### EXAMPLE 7.7

A high-speed car with  $m = 2000$  kg,  $C_D = 0.3$ , and  $A = 1$  m<sup>2</sup> deploys a 2-m parachute to slow down from an initial velocity of 100 m/s (Fig. E7.7). Assuming constant  $C_D$ , brakes free, and no rolling resistance, calculate the distance and velocity of the car after 1, 10, 100, and 1000 s. For air assume  $\rho = 1.2$  kg/m<sup>3</sup>, and neglect interference between the wake of the car and the parachute.



### Solution

Newton's law applied in the direction of motion gives

$$F_x = m \frac{dV}{dt} = -F_c - F_p = -\frac{1}{2} \rho V^2 (C_{Dc} A_c + C_{Dp} A_p)$$

where subscript  $c$  denotes the car and subscript  $p$  the parachute. This is of the form

$$\frac{dV}{dt} = -\frac{K}{m} V^2 \quad K = \sum C_D A \frac{\rho}{2}$$

Separate the variables and integrate

$$\int_{V_0}^V \frac{dV}{V^2} = -\frac{K}{m} \int_0^t dt$$

or

$$V_0^{-1} - V^{-1} = -\frac{K}{m} t$$

Rearrange and solve for the velocity  $V$ :

$$V = \frac{V_0}{1 + (K/m)V_0 t} \quad K = \frac{(C_{Dc} A_c + C_{Dp} A_p) \rho}{2} \quad (1)$$

We can integrate this to find the distance traveled:

$$S = \frac{V_0}{\alpha} \ln(1 + \alpha t) \quad \alpha = \frac{K}{m} V_0 \quad (2)$$

Now work out some numbers. From Table 7.3,  $C_{Dp} \approx 1.2$ ; hence

$$C_{Dc} A_c + C_{Dp} A_p = 0.3(1 \text{ m}^2) + 1.2 \frac{\pi}{4} (2 \text{ m})^2 = 4.07 \text{ m}^2$$

Then 
$$\frac{K}{m} V_0 = \frac{\frac{1}{2}(4.07 \text{ m}^2)(1.2 \text{ kg/m}^3)(100 \text{ m/s})}{2000 \text{ kg}} = 0.122 \text{ s}^{-1} = \alpha$$

Now make a table of the results for  $V$  and  $S$  from Eqs. (1) and (2):

|                  |    |     |      |      |
|------------------|----|-----|------|------|
| $t, \text{ s}$   | 1  | 10  | 100  | 1000 |
| $V, \text{ m/s}$ | 89 | 45  | 7.6  | 0.8  |
| $S, \text{ m}$   | 94 | 654 | 2110 | 3940 |

Air resistance alone will not stop a body completely. If you don't apply the brakes, you'll be halfway to the Yukon Territory and still going.

Other Methods of Drag Reduction

Sometimes drag is good, for example, when using a parachute. Do not jump out of an airplane holding a flat plate parallel to your motion (see Prob. 7.81). Mostly, though, drag is bad and should be reduced. The classical method of drag reduction is *streamlining* (Figs. 7.15 and 7.18). For example, nose fairings and body panels have produced motorcycles which can travel over 200 mi/h. More recent research has uncovered other methods which hold great promise, especially for turbulent flows.

1. Oil pipelines introduce an *annular core* of water to reduce the pumping power [36]. The low-viscosity water rides the wall and reduces friction up to 60 percent.
2. Turbulent friction in liquid flows is reduced up to 60 percent by dissolving small amounts of a *high-molecular-weight polymer additive* [37]. Without changing pumps, the Trans-Alaska Pipeline System (TAPS) increased oil flow 50 percent by injecting small amounts of polymer dissolved in kerosene.
3. Stream-oriented surface *vee-groove microriblets* reduce turbulent friction up to 8 percent [38]. Riblet heights are of order 1 mm and were used on the Stars and Stripes yacht hull in the Americas Cup races. Riblets are also effective on aircraft skins.
4. Small, near-wall *large-eddy breakup devices* (LEBUs) reduce local turbulent friction up to 10 percent [39]. However, one must add these small structures to the surface.
5. Air *microbubbles* injected at the wall of a water flow create a low-shear bubble blanket [40]. At high void fractions, drag reduction can be 80 percent.
6. Spanwise (transverse) *wall oscillation* may reduce turbulent friction up to 30 percent [41].

Drag reduction is presently an area of intense and fruitful research and applies to many types of airflows and water flows for both vehicles and conduits.

Drag of Surface Ships

The drag data above, such as Tables 7.2 and 7.3, are for bodies “fully immersed” in a free stream, i.e., with no free surface. If, however, the body moves at or near a free liquid surface, *wave-making drag* becomes important and is dependent upon both the Reynolds number and the Froude number. To move through a water surface, a ship

must create waves on both sides. This implies putting energy into the water surface and requires a finite drag force to keep the ship moving, even in a frictionless fluid. The total drag of a ship can then be approximated as the sum of friction drag and wave-making drag:

$$F \approx F_{\text{fric}} + F_{\text{wave}} \quad \text{or} \quad C_D \approx C_{D,\text{fric}} + C_{D,\text{wave}}$$

The friction drag can be estimated by the (turbulent) flat-plate formula, Eq. (7.45), based on the below-water or *wetted area* of the ship.

Reference 27 is an interesting review of both theory and experiment for wake-making surface ship drag. Generally speaking, the bow of the ship creates a wave system whose wavelength is related to the ship speed but not necessarily to the ship length. If the stern of the ship is a wave *trough*, the ship is essentially climbing uphill and has high wave drag. If the stern is a wave crest, the ship is nearly level and has lower drag. The criterion for these two conditions results in certain approximate Froude numbers [27]:

$$\text{Fr} = \frac{V}{\sqrt{gL}} \approx \frac{0.53}{\sqrt{N}} \quad \begin{array}{l} \text{high drag if } N = 1, 3, 5, 7, \dots; \\ \text{low drag if } N = 2, 4, 6, 8, \dots \end{array} \quad (7.65)$$

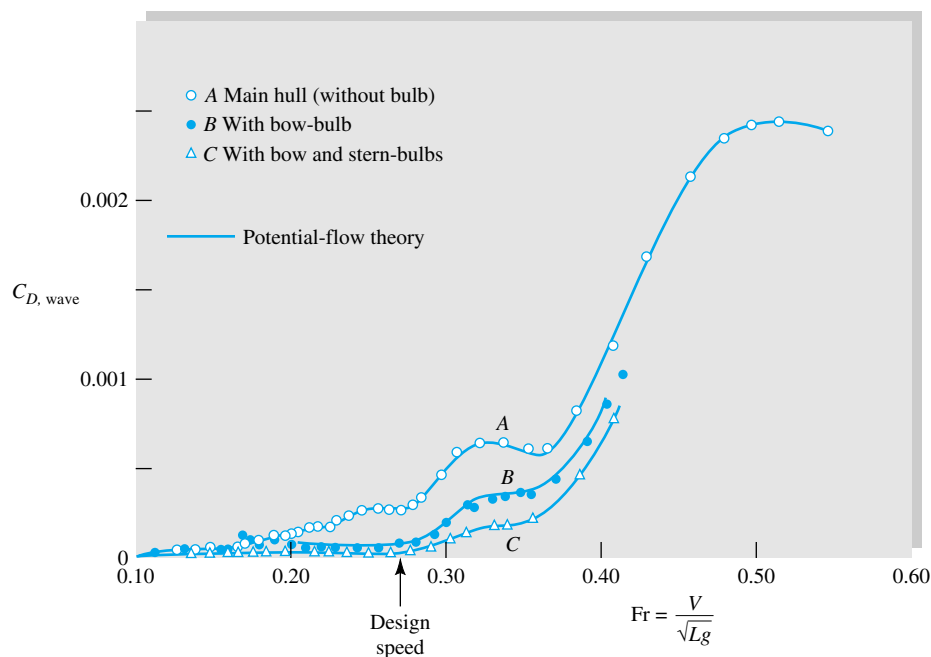
where  $V$  is the ship's speed,  $L$  is the ship's length along the centerline, and  $N$  is the number of half-lengths, from bow to stern, of the drag-making wave system. The wave drag will increase with the Froude number and oscillate between lower drag ( $\text{Fr} \approx 0.38, 0.27, 0.22, \dots$ ) and higher drag ( $\text{Fr} \approx 0.53, 0.31, 0.24, \dots$ ) with negligible variation for  $\text{Fr} < 0.2$ . Thus it is best to design a ship to cruise at  $N = 2, 4, 6, 8$ . Shaping the bow and stern can further reduce wave-making drag.

Figure 7.19 shows the data of Inui [27] for a model ship. The main hull, curve *A*, shows peaks and valleys in wave drag at the appropriate Froude numbers  $> 0.2$ . Introduction of a *bulb* protrusion on the bow, curve *B*, greatly reduces the drag. Adding a second bulb to the stern, curve *C*, is still better, and Inui recommends that the design speed of this two-bulb ship be at  $N = 4$ ,  $\text{Fr} \approx 0.27$ , which is a nearly “waveless” condition. In this figure  $C_{D,\text{wave}}$  is defined as  $2F_{\text{wave}}/(\rho V^2 L^2)$  instead of using the wetted area.

The solid curves in Fig. 7.19 are based on potential-flow theory for the below-water hull shape. Chapter 8 is an introduction to potential-flow theory. Modern digital computers can be programmed for numerical CFD solutions of potential flow over the hulls of ships, submarines, yachts, and sailboats, including boundary-layer effects driven by the potential flow [28]. Thus theoretical prediction of flow past surface ships is now at a fairly high level. See also Ref. 15.

## Body Drag at High Mach Numbers

All the data presented above are for nearly incompressible flows, with Mach numbers assumed less than about 0.5. Beyond this value compressibility can be very important, with  $C_D = \text{fcn}(\text{Re}, \text{Ma})$ . As the stream Mach number increases, at some subsonic value  $M_{\text{crit}} < 1$  which depends upon the body's bluntness and thickness, the local velocity at some point near the body surface will become sonic. If  $\text{Ma}$  increases beyond  $M_{\text{crit}}$ , shock waves form, intensify, and spread, raising surface pressures near the front of the body and therefore increasing the pressure drag. The effect can be dramatic with  $C_D$



**Fig. 7.19** Wave-making drag on a ship model. (After Inui [27].) *Note:* The drag coefficient is defined as  $C_{DW} = 2F/(\rho V^2 L^2)$ .

increasing tenfold, and 70 years ago this sharp increase was called the *sonic barrier*, implying that it could not be surmounted. Of course, it can be—the rise in  $C_D$  is finite, as supersonic bullets have proved for centuries.

Figure 7.20 shows the effect of the Mach number on the drag coefficient of various body shapes tested in air.<sup>5</sup> We see that compressibility affects blunt bodies earlier, with  $Ma_{crit}$  equal to 0.4 for cylinders, 0.6 for spheres, and 0.7 for airfoils and pointed projectiles. Also the Reynolds number (laminar versus turbulent boundary-layer flow) has a large effect below  $Ma_{crit}$  for spheres and cylinders but becomes unimportant above  $Ma \approx 1$ . In contrast, the effect of the Reynolds number is small for airfoils and projectiles and is not shown in Fig. 7.20. A general statement might divide Reynolds- and Mach-number effects as follows:

- $Ma \leq 0.4$ : Reynolds number important, Mach number unimportant
- $0.4 < Ma < 1$ : both Reynolds and Mach numbers important
- $Ma > 1.0$ : Reynolds number unimportant, Mach number important

At supersonic speeds, a broad *bow shock wave* forms in front of the body (see Figs. 9.10*b* and 9.19), and the drag is mainly due to high shock-induced pressures on the front. Making the bow a sharp point can sharply reduce the drag (Fig. 9.28) but does not eliminate the bow shock. Chapter 9 gives a brief treatment of compressibility. References 30 and 31 are more advanced textbooks devoted entirely to compressible flow.

<sup>5</sup>There is a slight effect of the specific-heat ratio  $k$  which would appear if other gases were tested.



## Biological Drag Reduction

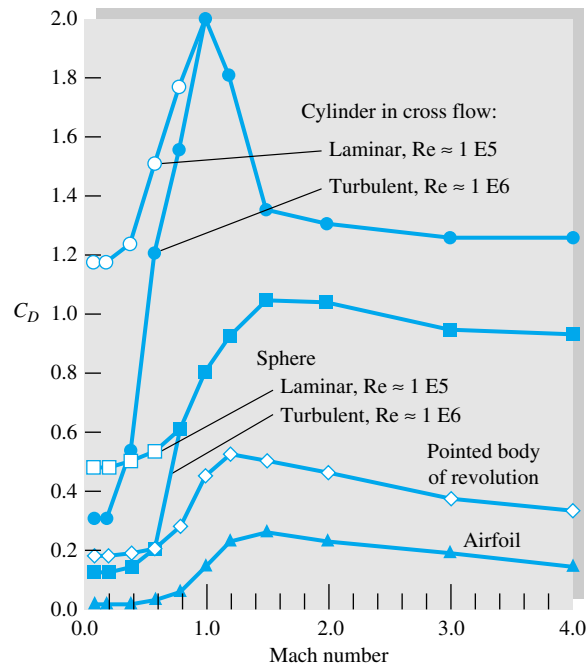
A great deal of engineering effort goes into designing immersed bodies to reduce their drag. Most such effort concentrates on rigid-body shapes. A different process occurs in nature, as organisms adapt to survive high winds or currents, as reported in a series of papers by S. Vogel [33, 34]. A good example is a tree, whose flexible structure allows it to reconfigure in high winds and thus reduce drag and damage. Tree root systems have evolved in several ways to resist wind-induced bending moments, and trunk cross sections have become resistant to bending but relatively easy to twist and reconfigure. We saw this in Table 7.3, where tree drag coefficients [24] reduced by 60 percent as wind velocity increased. The shape of the tree changes to offer less resistance.

The individual branches and leaves of a tree also curl and cluster to reduce drag. Figure 7.21 shows the results of wind tunnel experiments by Vogel [33]. A tulip tree leaf, Fig. 7.21(a), broad and open in low wind, curls into a conical low-drag shape as wind increases. A compound black walnut leaf group, Fig. 7.21(b), clusters into a low-drag shape at high wind speed. Although drag coefficients were reduced up to 50 percent by flexibility, Vogel points out that rigid structures are sometimes just as effective. An interesting recent symposium [35] was devoted entirely to the solid mechanics and fluid mechanics of biological organisms.

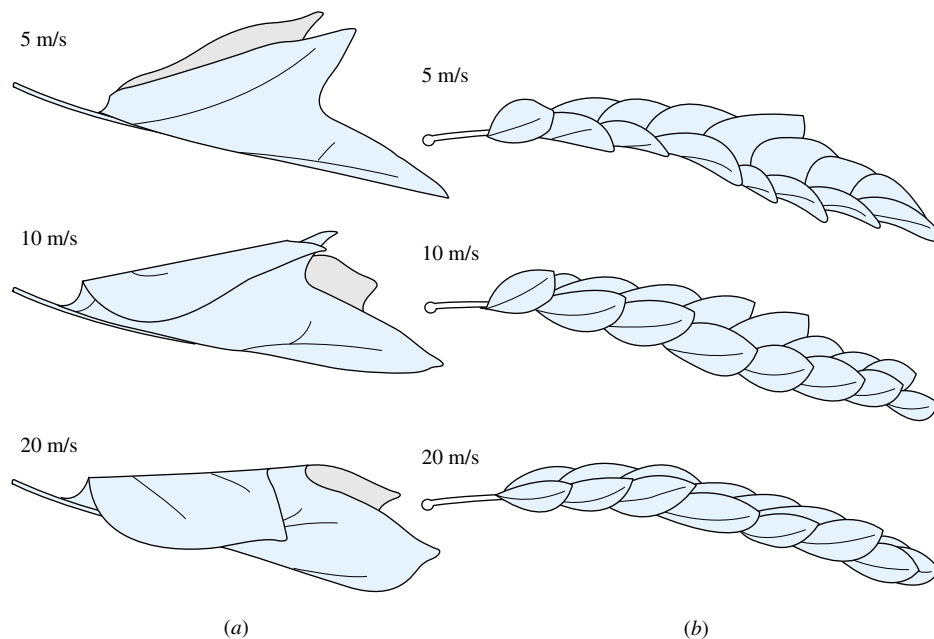
## Forces on Lifting Bodies

Lifting bodies (airfoils, hydrofoils, or vanes) are intended to provide a large force normal to the free stream and as little drag as possible. Conventional design practice has evolved a shape not unlike a bird's wing, i.e., relatively thin ( $t/c \leq 0/18$ ) with a rounded leading edge and a sharp trailing edge. A typical shape is sketched in Fig. 7.22.

For our purposes we consider the body to be symmetric, as in Fig. 7.11, with the



**Fig. 7.20** Effect of the Mach number on the drag of various body shapes. (Data from Refs. 23 and 29.)



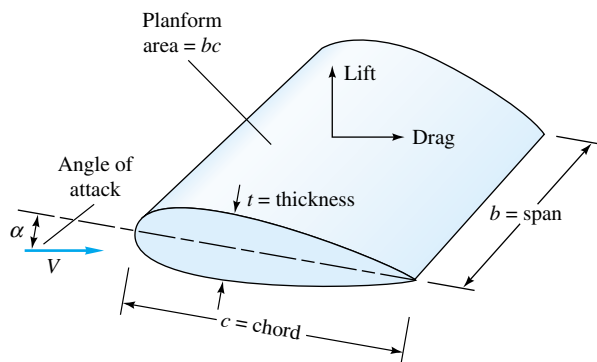
**Fig. 7.21** Biological adaptation to wind forces: (a) a tulip tree leaf curls into a conical shape at high velocity; (b) black walnut leaves cluster into a low-drag shape as wind increases. (From Vogel, Ref. 33.)

free-stream velocity in the vertical plane. If the chord line between the leading and trailing edge is not a line of symmetry, the airfoil is said to be *cambered*. The camber line is the line midway between the upper and lower surfaces of the vane.

The angle between the free stream and the chord line is called the *angle of attack*  $\alpha$ . The lift  $L$  and the drag  $D$  vary with this angle. The dimensionless forces are defined with respect to the planform area  $A_p = bc$ :

Lift coefficient: 
$$C_L = \frac{L}{\frac{1}{2}\rho V^2 A_p} \quad (7.66a)$$

Drag coefficient: 
$$C_D = \frac{D}{\frac{1}{2}\rho V^2 A_p} \quad (7.66b)$$



**Fig. 7.22** Definition sketch for a lifting vane.

If the chord length is not constant, as in the tapered wings of modern aircraft,  $A_p = \int c \, db$ .

For low-speed flow with a given roughness ratio,  $C_L$  and  $C_D$  should vary with  $\alpha$  and the chord Reynolds number

$$C_L = f(\alpha, Re_c) \quad \text{or} \quad C_D = f(\alpha, Re_c)$$

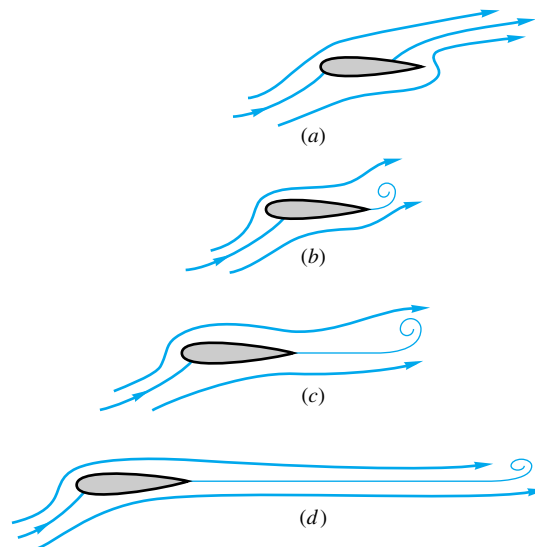
where  $Re_c = Vc/\nu$ . The Reynolds numbers are commonly in the turbulent-boundary-layer range and have a modest effect.

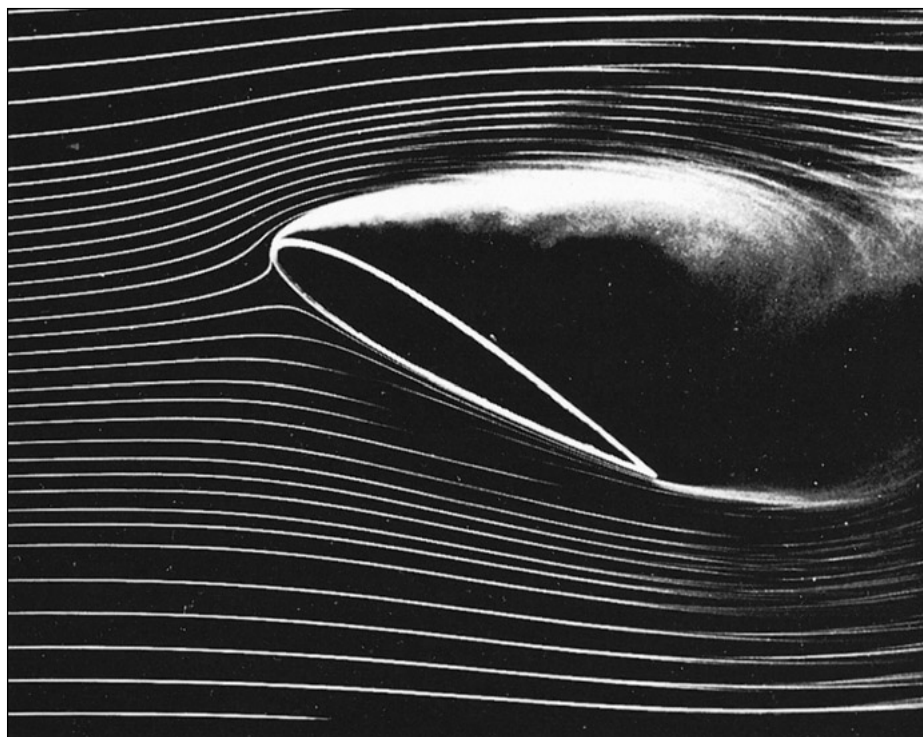
The rounded leading edge prevents flow separation there, but the sharp trailing edge causes a separation which generates the lift. Figure 7.23 shows what happens when a flow starts up past a lifting vane or an airfoil.

Just after start-up in Fig. 7.23a the streamline motion is irrotational and inviscid. The rear stagnation point, assuming a positive angle of attack, is on the upper surface, and there is no lift; but the flow cannot long negotiate the sharp turn at the trailing edge: it separates, and a *starting vortex* forms in Fig. 7.23b. This starting vortex is shed downstream in Fig. 7.23c and d, and a smooth streamline flow develops over the wing, leaving the foil in a direction approximately parallel to the chord line. Lift at this time is fully developed, and the starting vortex is gone. Should the flow now cease, a *stopping vortex* of opposite (clockwise) sense will form and be shed. During flight, increases or decreases in lift will cause incremental starting or stopping vortices, always with the effect of maintaining a smooth parallel flow at the trailing edge. We pursue this idea mathematically in Chap. 8.

At a low angle of attack, the rear surfaces have an adverse pressure gradient but not enough to cause significant boundary-layer separation. The flow pattern is smooth, as in Fig. 7.23d, and drag is small and lift excellent. As the angle of attack is increased, the upper-surface adverse gradient becomes stronger, and generally a *separation bub-*

**Fig. 7.23** Transient stages in the development of lift: (a) start-up: rear stagnation point on the upper surface: no lift; (b) sharp trailing edge induces separation, and a starting vortex forms: slight lift; (c) starting vortex is shed, and streamlines flow smoothly from trailing edge: lift is now 80 percent developed; (d) starting vortex now shed far behind, trailing edge now very smooth: lift fully developed.





**Fig. 7.24** At high angle of attack, smoke-flow visualization shows stalled flow on the upper surface of a lifting vane. [From Ref. 19, Illustrated Experiments in Fluid Mechanics (*The NCFMF Book of Film Notes*), National Committee for Fluid Mechanics Films, Education Development Center, Inc., copyright 1972.]

ble begins to creep forward on the upper surface.<sup>6</sup> At a certain angle  $\alpha = 15$  to  $20^\circ$ , the flow is separated completely from the upper surface, as in Fig. 7.24. The airfoil is said to be *stalled*: Lift drops off markedly, drag increases markedly, and the foil is no longer flyable.

Early airfoils were thin, modeled after birds' wings. The German engineer Otto Lilienthal (1848–1896) experimented with flat and cambered plates on a rotating arm. He and his brother Gustav flew the world's first glider in 1891. Horatio Frederick Phillips (1845–1912) built the first wind tunnel in 1884 and measured the lift and drag of cambered vanes. The first theory of lift was proposed by Frederick W. Lanchester shortly afterward. Modern airfoil theory dates from 1905, when the Russian hydrodynamicist N. E. Joukowski (1847–1921) developed a circulation theorem (Chap. 8) for computing airfoil lift for arbitrary camber and thickness. With this basic theory, as extended and developed by Prandtl and Kármán and their students, it is now possible to design a low-speed airfoil to satisfy particular surface-pressure distributions and boundary-layer characteristics. There are whole families of airfoil designs, notably those developed in the United States under the sponsorship of the NACA (now NASA). Extensive theory and data on these airfoils are contained in Ref. 16. We shall discuss this further in Chap. 8.

Figure 7.25 shows the lift and drag on a symmetric airfoil denoted as the NACA 0009 foil, the last digit indicating the thickness of 9 percent. With no flap extended,

<sup>6</sup>For some airfoils the bubble leaps, not creeps, forward, and stall occurs rapidly and dangerously.

this airfoil, as expected, has zero lift at zero angle of attack. Up to about  $12^\circ$  the lift coefficient increases linearly with a slope of 0.1 per degree, or 6.0 per radian. This is in agreement with the theory outlined in Chap. 8:

$$C_{L,\text{theory}} \approx 2\pi \sin\left(\alpha + \frac{2h}{c}\right) \quad (7.67)$$

where  $h/c$  is the maximum camber expressed as a fraction of the chord. The NACA 0009 has zero camber; hence  $C_L = 2\pi \sin \alpha \approx 0.11\alpha$ , where  $\alpha$  is in degrees. This is excellent agreement.

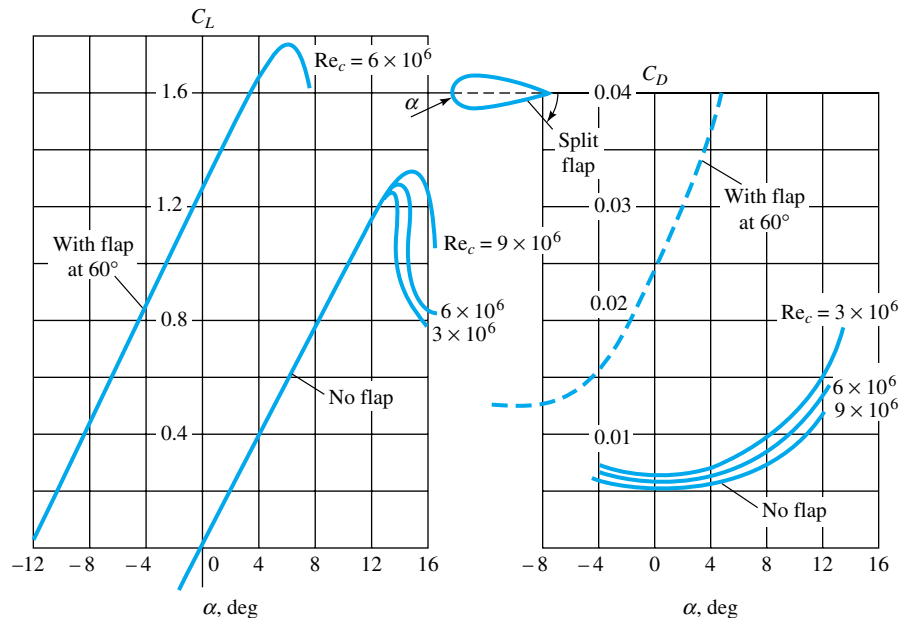
The drag coefficient of the smooth-model airfoils in Fig. 7.25 is as low as 0.005, which is actually lower than both sides of a flat plate in turbulent flow. This is misleading inasmuch as a commercial foil will have roughness effects; e.g., a paint job will double the drag coefficient.

The effect of increasing Reynolds number in Fig. 7.25 is to increase the maximum lift and stall angle (without changing the slope appreciably) and to reduce the drag coefficient. This is a salutary effect, since the prototype will probably be at a higher Reynolds number than the model ( $10^7$  or more).

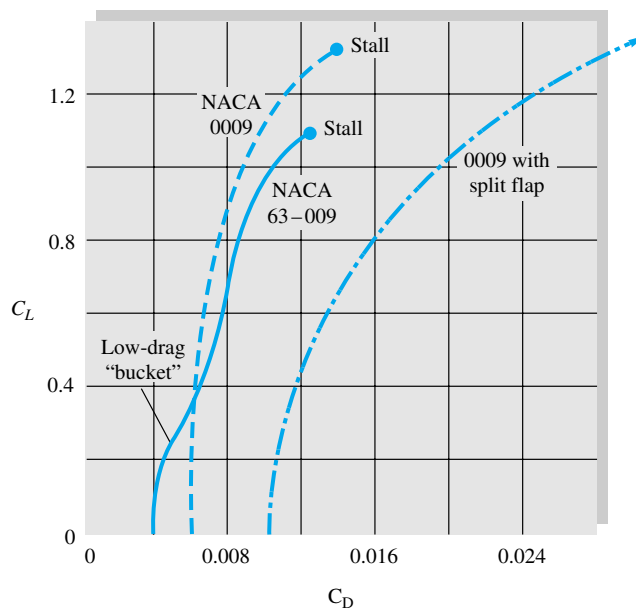
For takeoff and landing, the lift is greatly increased by deflecting a split flap, as shown in Fig. 7.25. This makes the airfoil unsymmetric (or effectively cambered) and changes the zero-lift point to  $\alpha = -12^\circ$ . The drag is also greatly increased by the flap, but the reduction in takeoff and landing distance is worth the extra power needed.

A lifting craft cruises at low angle of attack, where the lift is much larger than the drag. Maximum lift-to-drag ratios for the common airfoils lie between 20 and 50.

Some airfoils, such as the NACA 6 series, are shaped to provide favorable gradients over much of the upper surface at low angles. Thus separation is small, and transition to turbulence is delayed; the airfoil retains a good length of laminar flow even



**Fig. 7.25** Lift and drag of a symmetric NACA 0009 airfoil of infinite span, including effect of a split-flap deflection. Note that roughness can increase  $C_D$  from 100 to 300 percent.



**Fig. 7.26** Lift-drag polar plot for standard (0009) and a laminar-flow (63-009) NACA airfoil.

at high Reynolds numbers. The lift-drag polar plot in Fig. 7.26 shows the NACA 0009 data from Fig. 7.25 and a laminar-flow airfoil, NACA 63-009, of the same thickness. The laminar-flow airfoil has a low-drag bucket at small angles but also suffers lower stall angle and lower maximum lift coefficient. The drag is 30 percent less in the bucket, but the bucket disappears if there is significant surface roughness.

All the data in Figs. 7.25 and 7.26 are for infinite span, i.e., a two-dimensional flow pattern about wings without tips. The effect of finite span can be correlated with the dimensionless slenderness, or *aspect ratio*, denoted (AR),

$$AR = \frac{b^2}{A_p} = \frac{b}{\bar{c}} \quad (7.68)$$

where  $\bar{c}$  is the average chord length. Finite-span effects are shown in Fig. 7.27. The lift slope decreases, but the zero-lift angle is the same; and the drag increases, but the zero-lift drag is the same. The theory of finite-span airfoils [16] predicts that the effective angle of attack increases, as in Fig. 7.27, by the amount

$$\Delta\alpha \approx \frac{C_L}{\pi AR} \quad (7.69)$$

When applied to Eq. (7.67), the finite-span lift becomes

$$C_L \approx \frac{2\pi \sin(\alpha + 2h/c)}{1 + 2/AR} \quad (7.70)$$

The associated drag increase is  $\Delta C_D \approx C_L \sin \Delta\alpha \approx C_L \Delta\alpha$ , or

$$C_D \approx C_{D\infty} + \frac{C_L^2}{\pi AR} \quad (7.71)$$

where  $C_{D\infty}$  is the drag of the infinite-span airfoil, as sketched in Fig. 7.25. These correlations are in good agreement with experiments on finite-span wings [16].

The existence of a maximum lift coefficient implies the existence of a minimum speed, or *stall speed*, for a craft whose lift supports its weight

$$L = W = C_{L,\max}(\tfrac{1}{2}\rho V_s^2 A_p)$$

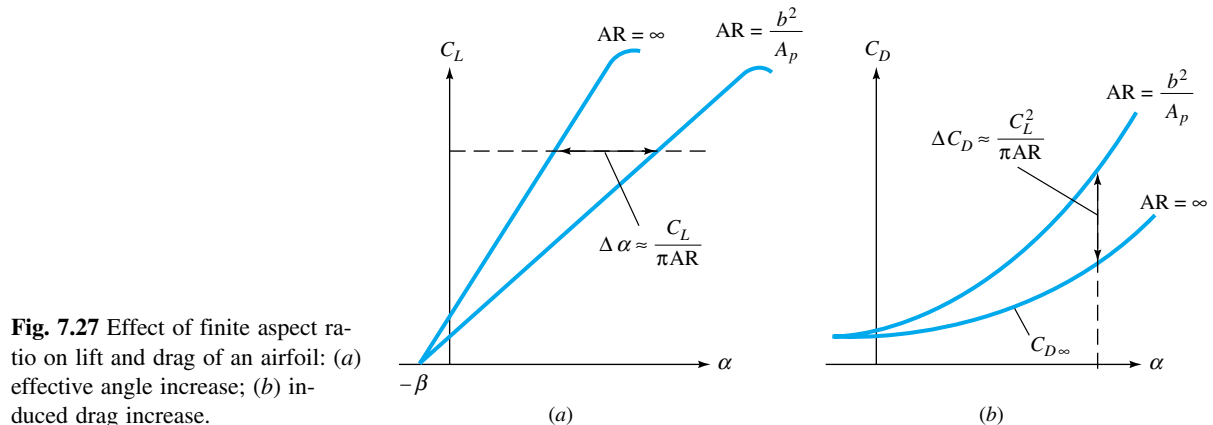
$$\text{or} \quad V_s = \left( \frac{2W}{C_{L,\max}\rho A_p} \right)^{1/2} \quad (7.72)$$

The stall speed of typical aircraft varies between 60 and 200 ft/s, depending upon the weight and value of  $C_{L,\max}$ . The pilot must hold the speed greater than about  $1.2V_s$  to avoid the instability associated with complete stall.

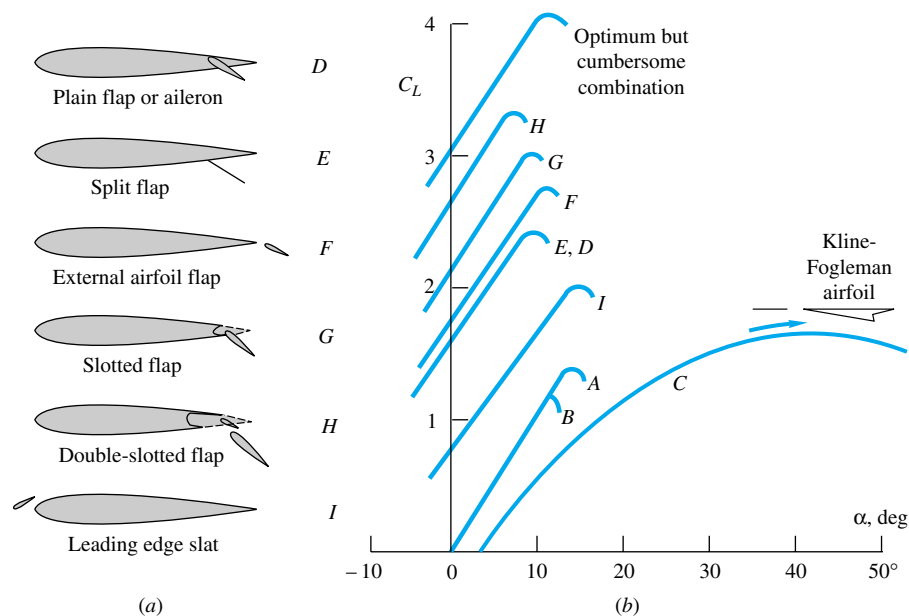
The split flap in Fig. 7.25 is only one of many devices used to secure high lift at low speeds. Figure 7.28a shows six such devices whose lift performance is given in 7.28b along with a standard (A) and laminar-flow (B) airfoil. The double-slotted flap achieves  $C_{L,\max} \approx 3.4$ , and a combination of this plus a leading-edge slat can achieve  $C_{L,\max} \approx 4.0$ . These are not scientific curiosities; e.g., the Boeing 727 commercial jet aircraft uses a triple-slotted flap plus a leading-edge slat during landing.

Also shown as C in Fig. 7.28b is the Kline-Fogleman airfoil [17], not yet a reality. The designers are amateur model-plane enthusiasts who did not know that conventional aerodynamic wisdom forbids a sharp leading edge and a step cutout from the trailing edge. The Kline-Fogleman airfoil has relatively high drag but shows an amazing continual increase in lift out to  $\alpha = 45^\circ$ . In fact, we may fairly say that this airfoil does not stall and provides smooth performance over a tremendous range of flight conditions. No explanation for this behavior has yet been published by any aerodynamicist. This airfoil is under study and may or may not have any commercial value.

Another violation of conventional aerodynamic wisdom is that military aircraft are beginning to fly, briefly, *above the stall point*. Fighter pilots are learning to make quick maneuvers in the stalled region as detailed in Ref. 32. Some planes can even *fly continuously* while stalled—the Grumman X-29 experimental aircraft recently set a record by flying at  $\alpha = 67^\circ$ .



**Fig. 7.27** Effect of finite aspect ratio on lift and drag of an airfoil: (a) effective angle increase; (b) induced drag increase.

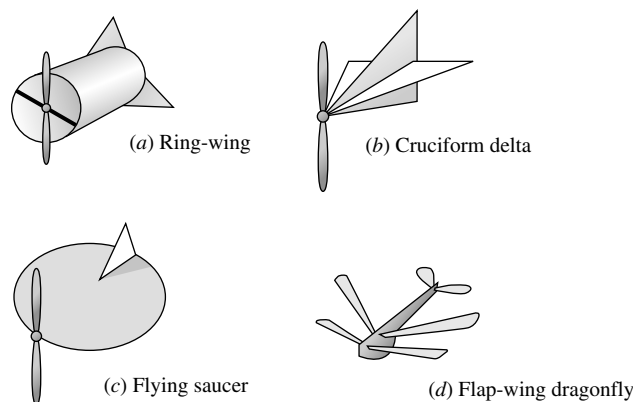


**Fig. 7.28** Performance of airfoils with and without high-lift devices:  $A = \text{NACA } 0009$ ;  $B = \text{NACA } 63-009$ ;  $C = \text{Kline-Fogleman airfoil}$  (from Ref. 17);  $D$  to  $I$  shown in (a); (a) types of high-lift devices; (b) lift coefficients for various devices.

## New Aircraft Designs

The Kline-Fogleman airfoil in Fig. 7.28 is a departure from conventional aerodynamics, but there have been other striking departures, as detailed in a recent article [42]. These new aircraft, conceived presently as small models, have a variety of configurations, as shown in Fig. 7.29: ring-wing, cruciform, flying saucer, and flap-wing. A saucer configuration (Fig. 7.29c), with a diameter of 40 in, has been successfully flown by radio control, and its inventor, Jack M. Jones, plans for a 20-ft two-passenger version. Another 18-in-span microplane called the Bat (not shown), made by MLB Co., flies for 20 min at 40 mi/h and contains a video camera for surveillance. New engines have been reduced to a 10- by 3-mm size, producing 20 W of power. At the other end of the size spectrum, Boeing and NASA engineers have proposed a jumbo flying-wing jetliner, similar in shape to the stealth bomber, which would carry 800 passengers for a range of 7000 mi.

Further information on the performance of lifting craft can be found in Refs. 12, 13, and 16. We discuss this matter again briefly in Chap. 8.



**Fig. 7.29** New aircraft designs do not necessarily look like your typical jetliner. (From Ref. 42.)



**EXAMPLE 7.8**

An aircraft weighs 75,000 lb, has a planform area of 2500 ft<sup>2</sup>, and can deliver a constant thrust of 12,000 lb. It has an aspect ratio of 7, and  $C_{D\infty} \approx 0.02$ . Neglecting rolling resistance, estimate the takeoff distance at sea level if takeoff speed equals 1.2 times stall speed. Take  $C_{L,\max} = 2.0$ .

**Solution**

The stall speed from Eq. (7.72), with sea-level density  $\rho = 0.00237$  slug/ft<sup>3</sup>, is

$$V_s = \left( \frac{2W}{C_{L,\max}\rho A_p} \right)^{1/2} = \left[ \frac{2(75,000)}{2.0(0.00237)(2500)} \right]^{1/2} = 112.5 \text{ ft/s}$$

Hence takeoff speed  $V_0 = 1.2V_s = 135$  ft/s. The drag is estimated from Eq. (7.71) for AR = 7 as

$$C_D \approx 0.02 + \frac{C_L^2}{7\pi} = 0.02 + 0.0455C_L^2$$

A force balance in the direction of takeoff gives

$$F_s = m \frac{dV}{dt} = \text{thrust} - \text{drag} = T - kV^2 \quad k = \frac{1}{2}C_D\rho A_p \quad (1)$$

Since we are looking for distance, not time, we introduce  $dV/dt = V dV/ds$  into Eq. (1), separate variables, and integrate

$$\int_0^{S_0} dS = \frac{m}{2} \int_0^{V_0} \frac{d(V^2)}{T - kV^2} \quad k \approx \text{const}$$

$$\text{or} \quad S_0 = \frac{m}{2k} \ln \frac{T}{T - kV_0^2} = \frac{m}{2k} \ln \frac{T}{T - D_0} \quad (2)$$

where  $D_0 = kV_0^2$  is the takeoff drag. Equation (2) is the desired theoretical relation for takeoff distance. For the particular numerical values, take

$$m = \frac{75,000}{32.2} = 2329 \text{ slugs}$$

$$C_{L_0} = \frac{W}{\frac{1}{2}\rho V_0^2 A_p} = \frac{75,000}{\frac{1}{2}(0.00237)(135)^2(2500)} = 1.39$$

$$C_{D_0} = 0.02 + 0.0455(C_{L_0})^2 = 0.108$$

$$k \approx \frac{1}{2}C_{D_0}\rho A_p = (\frac{1}{2})(0.108)(0.00237)(2500) = 0.319 \text{ slug/ft}$$

$$D_0 = kV_0^2 = 5820 \text{ lb}$$

Then Eq. (2) predicts that

$$S_0 = \frac{2329 \text{ slugs}}{2(0.319 \text{ slug/ft})} \ln \frac{12,000}{12,000 - 5820} = 3650 \ln 1.94 = 2420 \text{ ft} \quad \text{Ans.}$$

A more exact analysis accounting for variable  $k$  [13] gives the same result to within 1 percent.

Summary

This chapter has dealt with viscous effects in external flow past bodies immersed in a stream. When the Reynolds number is large, viscous forces are confined to a thin boundary layer and wake in the vicinity of the body. Flow outside these “shear layers” is essentially inviscid and can be predicted by potential theory and Bernoulli’s equation.

The chapter begins with a discussion of the flat-plate boundary layer and the use of momentum-integral estimates to predict the wall shear, friction drag, and thickness of such layers. These approximations suggest how to eliminate certain small terms in the Navier-Stokes equations, resulting in Prandtl’s boundary-layer equations for laminar and turbulent flow. Section 7.4 then solves the boundary-layer equations to give very accurate formulas for flat-plate flow at high Reynolds numbers. Rough-wall effects are included, and Sec. 7.5 gives a brief introduction to pressure-gradient effects. An adverse (decelerating) gradient is seen to cause flow separation, where the boundary layer breaks away from the surface and forms a broad, low-pressure wake.

Boundary-layer theory fails in separated flows, which are commonly studied by experiment. Section 7.6 gives data on drag coefficients of various two- and three-dimensional body shapes. The chapter ends with a brief discussion of lift forces generated by lifting bodies such as airfoils and hydrofoils. Airfoils also suffer flow separation or *stall* at high angles of incidence.

Problems

Most of the problems herein are fairly straightforward. More difficult or open-ended assignments are labeled with an asterisk. Problems labeled with an EES icon will benefit from the use of the Engineering Equation Solver (EES), while problems labeled with a computer disk may require the use of a computer. The standard end-of-chapter problems 7.1 to 7.124 (categorized in the problem list below) are followed by word problems W7.1 to W7.12, fundamentals of engineering exam problems FE7.1 to FE7.10, comprehensive problems C7.1 to C7.4, and design project D7.1.

Problem Distribution

| Section | Topic                                  | Problems    |
|---------|--|-------------|
| 7.1     | Reynolds-number and geometry           | 7.1–7.5     |
| 7.2     | Momentum-integral estimates            | 7.6–7.12    |
| 7.3     | The boundary-layer equations           | 7.13–7.15   |
| 7.4     | Laminar flat-plate flow                | 7.16–7.29   |
| 7.4     | Turbulent flat-plate flow              | 7.30–7.46   |
| 7.5     | Boundary layers with pressure gradient | 7.47–7.52   |
| 7.6     | Drag of two-dimensional bodies         | 7.53–7.63   |
| 7.6     | Drag of three-dimensional bodies       | 7.64–7.114  |
| 7.6     | Lifting bodies—airfoils                | 7.115–7.124 |

- P7.1** For flow at 20 m/s past a thin flat plate, estimate the distances  $x$  from the leading edge at which the boundary-layer thickness will be either 1 mm or 10 cm for (a) air and (b) water at 20°C and 1 atm.

**P7.2** Air, equivalent to that at a standard altitude of 4000 m, flows at 450 mi/h past a wing which has a thickness of 18

cm, a chord length of 1.5 m, and a wingspan of 12 m. What is the appropriate value of the Reynolds number for correlating the lift and drag of this wing? Explain your selection.

- P7.3** Equation (7.1b) assumes that the boundary layer on the plate is turbulent from the leading edge onward. Devise a scheme for determining the boundary-layer thickness more accurately when the flow is laminar up to a point  $Re_{x,crit}$  and turbulent thereafter. Apply this scheme to computation of the boundary-layer thickness at  $x = 1.5$  m in 40 m/s flow of air at 20°C and 1 atm past a flat plate. Compare your result with Eq. (7.1b). Assume  $Re_{x,crit} \approx 1.2 E6$ .

**P7.4** Air at 20°C and 1 atm flows at 15 m/s past a flat plate with  $Re_{x,crit} \approx 1 E6$ . At what point  $x$  will the boundary-layer thickness be 8 mm? Why do Eqs. (7.1) seem to fail? Make a sketch illustrating the discrepancy; then use the ideas in Prob. 7.3 to complete this problem correctly.

**P7.5** SAE 30 oil at 20°C flows at 1.8 ft<sup>3</sup>/s from a reservoir into a 6-in-diameter pipe. Use flat-plate theory to estimate the position  $x$  where the pipe-wall boundary layers meet in the center. Compare with Eq. (6.5), and give some explanations for the discrepancy.

**P7.6** For the laminar parabolic boundary-layer profile of Eq. (7.6), compute the shape factor  $H$  and compare with the exact Blasius result, Eq. (7.31).

**P7.7** Air at 20°C and 1 atm enters a 40-cm-square duct as in Fig. P7.7. Using the “displacement thickness” concept of Fig. 7.4, estimate (a) the mean velocity and (b) the mean pressure in the core of the flow at the position  $x =$